AD-A096 561 NAVAL RESEARCH LAB WASHINGTON DC F/G 20/8
HIGH IMPEDANCE ION DIODE EXPERIMENT ON AURORA.(U)
MAR 81 R A MEGER, F C YOUNG, A T DROBOT
UNCLASSIFIED NRL-MR-4477 NL

1 OF 1
AD A096561

END
DATE FILMED
4-81
DTIC

SECURITY CLASSIFICATION OF THIS PAGE *(When Data Entered)*

REPORT DOCUMENTATION PAGE	READ INSTRUCTIONS BEFORE COMPLETING FORM
1. REPORT NUMBER: NRL Memorandum Report 4477 — 2. GOVT ACCESSION NO.: AD-A096561	3. RECIPIENT'S CATALOG NUMBER
4. TITLE *(and Subtitle)*: HIGH IMPEDANCE ION DIODE EXPERIMENT ON AURORA	5. TYPE OF REPORT & PERIOD COVERED: Interim report on a continuing NRL problem.
	6. PERFORMING ORG. REPORT NUMBER
7. AUTHOR(s): R. A. Meger*, F. C. Young, A. T. Drobot†, G. Cooperstein, Shyke A. Goldstein*, D. Mosher, S. E. Graybill**, G. A. Huttlin**, K. G. Kerris**, and A. G. Stewart**	8. CONTRACT OR GRANT NUMBER(s)
9. PERFORMING ORGANIZATION NAME AND ADDRESS: Naval Research Laboratory, Washington, DC 20375	10. PROGRAM ELEMENT, PROJECT, TASK AREA & WORK UNIT NUMBERS: 47-0875-0-1
11. CONTROLLING OFFICE NAME AND ADDRESS: Defense Nuclear Agency, Washington, DC 20305	12. REPORT DATE: March 19, 1981
	13. NUMBER OF PAGES: 67
14. MONITORING AGENCY NAME & ADDRESS*(if different from Controlling Office)*	15. SECURITY CLASS. *(of this report)*: UNCLASSIFIED
	15a. DECLASSIFICATION/DOWNGRADING SCHEDULE

16. DISTRIBUTION STATEMENT *(of this Report)*

Approved for public release; distribution unlimited.

17. DISTRIBUTION STATEMENT *(of the abstract entered in Block 20, if different from Report)*

18. SUPPLEMENTARY NOTES

This research was sponsored in part by the Defense Nuclear Agency under Subtask T99QAXLA014, work unit 46, and work unit title "Ion Beam Generation".

*Present address: JAYCOR, Alexandria, VA 22304
†Present address: Science Applications Inc., McLean, VA 22102
**Present address: Harry Diamond Laboratories, Adelphi, MD 20783

19. KEY WORDS *(Continue on reverse side if necessary and identify by block number)*

20. ABSTRACT *(Continue on reverse side if necessary and identify by block number)*

An ion diode experiment has been performed on the Aurora accelerator. Average proton currents of ~ 50 kA at 5 MeV have been inferred from nuclear diagnostics. Computer simulations agree with the experimental results.

DD FORM 1 JAN 73 1473 EDITION OF 1 NOV 65 IS OBSOLETE
S/N 0102-LF-014-6601

SECURITY CLASSIFICATION OF THIS PAGE *(When Data Entered)*

CONTENTS

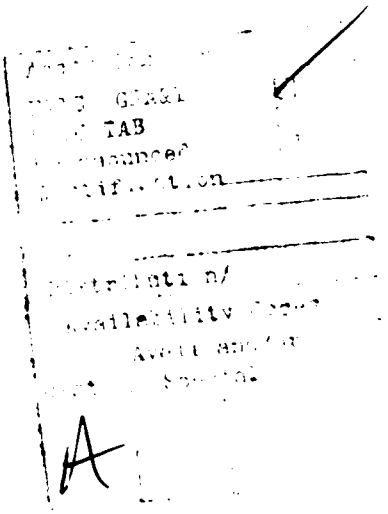

I. INTRODUCTION

There is increasing interest in the development of intense light-ion beams as drivers for thermonuclear pellets in inertial-confinement-fusion (ICF) applications.[1,2] This approach requires the production of a number of intense beams of a few MeV/nucleon, focusing of each beam, then transport and overlapping of the beams onto a target with sufficient power density to ignite it. Experimental and theoretical research in these areas at the Naval Research Laboratory has been reviewed recently.[1]

The NRL studies have concentrated on the azimuthally-symmetric pinch-reflex diode for ion production. This diode uses the self-fields of the charged-particle flow to enhance ion production and aid in focusing. This diode operates most efficiently with a large aspect ratio (cathode radius/anode-cathode gap) and at low diode impedance ($Z \lesssim 2\Omega$).[3] Experiments on the 1.5-Ω NRL Gamble II generator have produced up to 700 kA of ion current at 1.3 MV with 60% ion efficiency (ion current/total current).[1] Using the 0.75-Ω line of the PITHON generator at Physics International, ion currents of 900 kA at 1.8 MV were achieved with comparable efficiency.[4,5] The high current density associated with these low-voltage, high-current ion beams puts limitations on the focusing and transport of such beams to ICF targets.[6,7]

Experiments at order-of-magnitude-higher impedance levels and at power levels comparable to Gamble II and PITHON experiments are now in progress on one line of the Harry Diamond Laboratories Aurora generator. In general, higher impedance generators are more efficient in delivering energy to the diode and can deliver higher power levels. Inductive losses in the vacuum diode are reduced. The increased stiffness of beams extracted from high-impedance diodes should improve focusability. Focused current densities required for pellet driving are reduced for higher-energy ion beams provided that the beam species is properly matched to pellet deposition requirements.

Manuscript submitted January 16, 1981.

These advantages must be weighed against theoretical predictions of lower ion production efficiencies for high impedance diodes.

The experiments described here employed a low-aspect-ratio modification of the conventional pinch-reflex diode in order to better match the high-impedance Aurora pulse-line. Computer simulation of the Aurora diode showed enhanced ion production when operating at diode currents exceeding the Alfven current. Aurora experiments have demonstrated similar enhanced ion production efficiencies ($\sim$ 25%). The ion diode was driven by a 200 nsec FWHM pulse from one of the 50-Ω vacuum transmission lines on the generator. The diode operated at $\sim$ 5 MV and $\sim$ 200 kA ($Z \sim 25\ \Omega$). The mismatch of this ion diode to the 50-Ω driver limited the peak power to < 1.5 TW and the total diode energy to < 200 kJ. Average proton currents of 50 kA at 5 MeV were inferred from neutron activation and time-of-flight measurements using the $^{7}Li(p,n)^{7}Be$ reaction. A carbon ion component of >1% was also observed from the CH_2 foil anode. Ion imaging measurements indicated that the ion beam originated near the axis of the anode and was affected by an unknown focusing mechanism in the anode-cathode region. It was shown that the reflexing of electrons through the anode foil was not of primary importance to the enhanced ion production. The experimental results are consistent with computer simulations which indicate that the ion production is enhanced as a result of prolonged electron-lifetime in the diode due to the complicated trajectories of the electrons.

This paper will detail the theoretical simulations and experimental measurements of these ion-diode studies on the Aurora generator in negative polarity. Section II presents the results of the numerical simulations. Section III describes the experimental hardware and diagnostics.

The experimental results are presented in Section IV. Section V summarizes the experimental and theoretical studies.

II. THEORY AND SIMULATION

The high impedance diode used in the Aurora experiments exhibits an ion production efficiency much higher than the prediction from bi-polar Child-Langmuir flow. The most important aspect of the flow established in the diode is that the total current, I_{TOT}, exceeds the Alfvén current, $I_A = 17000\ \beta\gamma$, where I_A is in amps, β is the electron velocity normalized to the speed of light and γ is the relativistic factor calculated from the full diode voltage. When the total diode current exceeds the Alfvén current, the electron flow pinches in the region of the anode-cathode gap. The electrons no longer have trajectories which take them directly from the cathode to the anode; rather they appear to perform complicated figure-eight-like orbits through the diode's axis and drift across the gap due to a combination of $\overline{E}\times\overline{B}$ and $\overline{\nabla}B\times\overline{B}$ motion caused by the self-magnetic field arising from the electron and ion flow in the diode. As a result, the electron lifetime in the anode-cathode gap is enhanced. The ion production efficiency is determined by the total charge balance in the diode and the relative average lifetimes of electrons and ions in the gap. The ions travel in essentially straight lines and move more slowly than the relativistic electrons, but the longer path length of the electrons allows a larger fraction of the current than predicted by Child-Langmuir theory to be carried by the ions.

For the diode used in the Aurora experiments, it is difficult to calculate analytically the ion-generation efficiency. Therefore, numerical simulations were used to model the diode behavior. These simulations have

been carried out using the DIODEPR 2D-3V relativistic-quasistatic equilibrium code. The configuration used in the simulations is shown in Fig. 1. This figure also shows the equipotential lines in the empty diode under the assumption that the reflexing foil is a conducting surface. This geometry corresponds to a small-aspect-ratio, pinch-reflex-diode configuration. To limit the size of the simulation grid, only the region to the right of the cathode was simulated thus neglecting the effect of shank flow into the diode. The numerical model assumed a geometry close to that used in the Aurora experiments. The "reflexing foil" was modeled as an 0.175-cm thick CH_2 conducting disk acting as a space-charge-limited ion source on the cathode side. The on-axis rod and the anode support behind the foil were assumed to be perfectly absorbing surfaces for electrons. Simulations were conducted on a (64×50) R-Z mesh with $\Delta R = 0.25$ cm and $\Delta Z = 0.15$ cm. The time step was taken to be 2×10^{-12} sec, and the simulations were conducted until an average steady state was achieved. Electron emission was limited to the face of the cathode. Two simulations were completed, one at 3 MeV and another at 5 MeV, both with an anode-cathode gap of 3.3 cm.

In the simulation at 3 MeV, the steady-state diode current was calculated to be 114 kA with 14 kA of this current due to ions and the remaining 100 kA due to electrons. Of the electron current, 35 kA was absorbed by the sides of the supporting rod, while 50 kA was absorbed by the front surface of the anode at the center button where the anode foil is attached to the support rod. The remaining current was absorbed by the back plate behind the support stalk. The positions of the electrons projected on the R-Z plane are shown in Fig. 2 at time step 3000, well after a steady state has been achieved. The electron flow appears to be weakly pinched and there is evidence of some reflexing through the anode foil. The

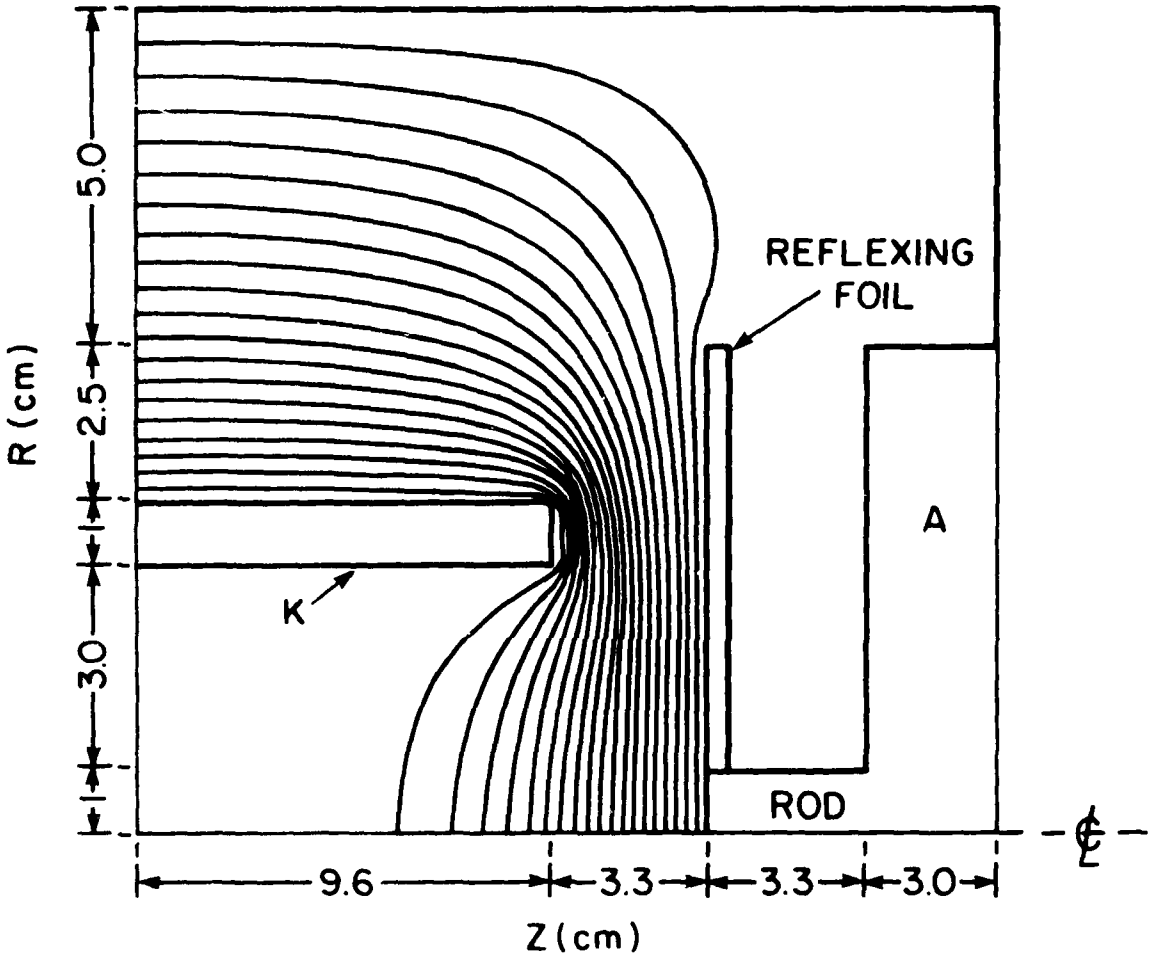

Fig. 1 The pinch-reflex-diode geometry used for simulation of the Aurora experiments. The equipotential lines in the empty diode are shown. Only the region to the right of the hollow cathode was simulated.

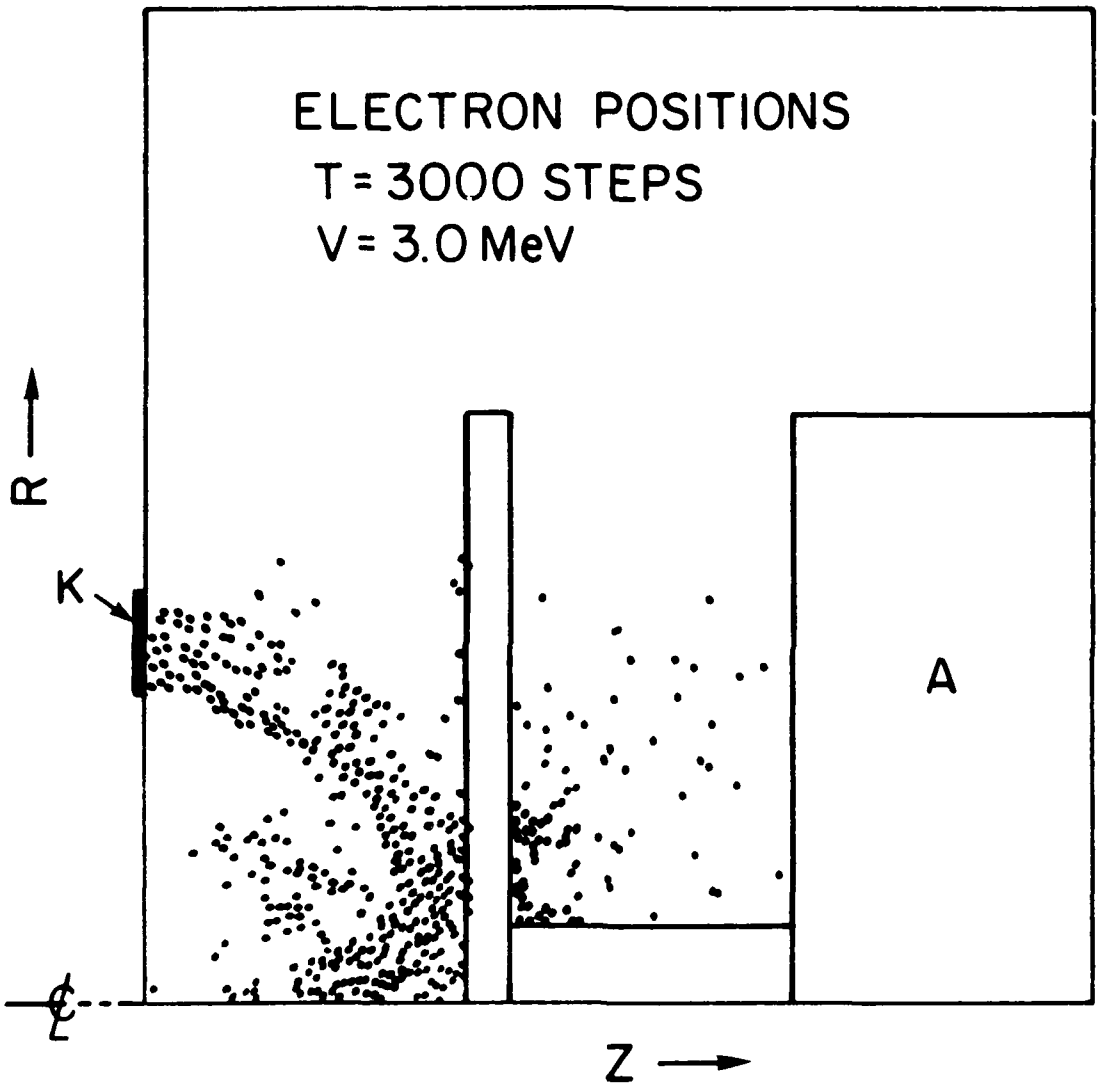

Fig. 2 – The positions of test electrons projected on the (R,Z) plane after 3000 timesteps. At this time the electron flow has reached steady state. This figure is for the 3-MeV case and shows a weak pinch of the electron flow.

corresponding ion positions appear in Fig. 3. The ion current density is peaked near the axis as can be seen from the radial profile for the ions at the cathode surface shown in Fig. 4. Within the resolution of the code, the peak ion density is $\sim$ 1 kA/cm^2. Ions arriving at the cathode face have an outward radial velocity with a maximum $v_R \sim 0.6$ cm/ns as shown in Fig. 5 compared to $v_Z \sim 2.3$ cm/ns indicating a defocusing of the ion orbits. The impedance of the diode was calculated to be 26 Ω with an ion efficiency of 12%, which is 2.5 times greater than the Child-Langmuir efficiency.

At the higher voltage of 5 MeV, the calculated ion-diode performance improves. Plots similar to those for 3 MeV show that the electron pinch is stronger at 5 MeV and that very few electrons reflex through the anode foil. The electron and ion maps are shown in Figs. 6 and 7, respectively, after 4000 time steps when the diode has achieved steady state. The electron flow appears to pinch toward the center of the anode face and very few electrons have passed through the foil. There also appears to be a sizeable electron flow in the direction of the ions which would contribute to space charge neutralization within the ion beam. The ion density on the cathode plane shown in Fig. 8 is strongly peaked on axis with a current density of at least 10 kA/cm^2 compared to 1 kA/cm^2 computed for 3-MeV operation. The total diode current for this case is 205 kA of which 40 kA is ion current and 165 kA is electron current. Of the electron current, 40 kA goes to the support rod and 125 kA to the center button. None of the electron current was absorbed by the back plate behind the anode stalk. In contrast to the 3-MeV case, this total current now exceeds the Alfvén current of 188 kA. The diode impedance of 24 Ω was not significantly different from the 3-MeV case, but the ion efficiency increased to $\sim$ 20%. The maximum radial velocity component, v_R, shown in Fig. 9, is somewhat

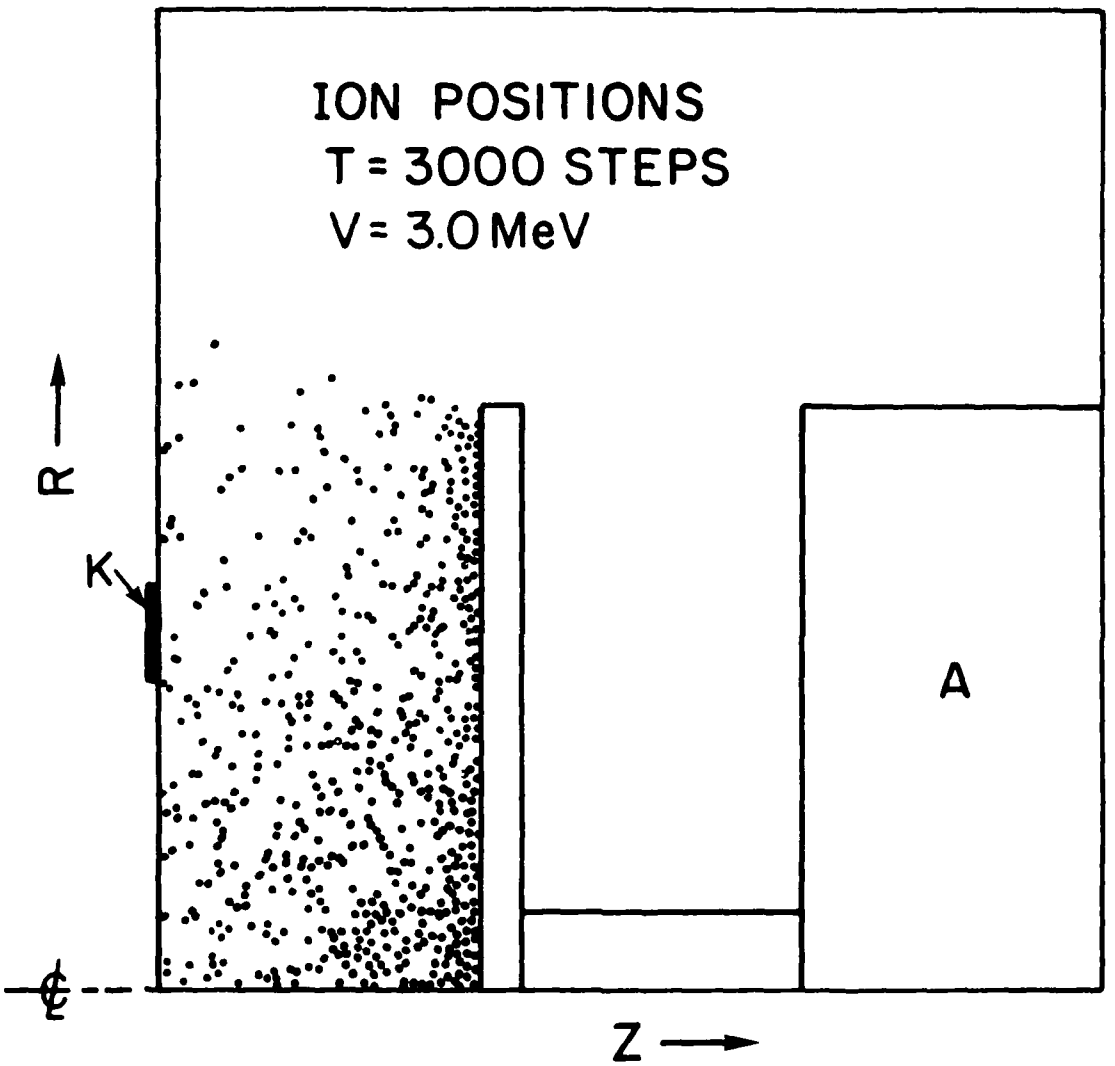

Fig. 3 — The positions of test ions projected onto the (R,Z) plane for the case shown in Fig. 2

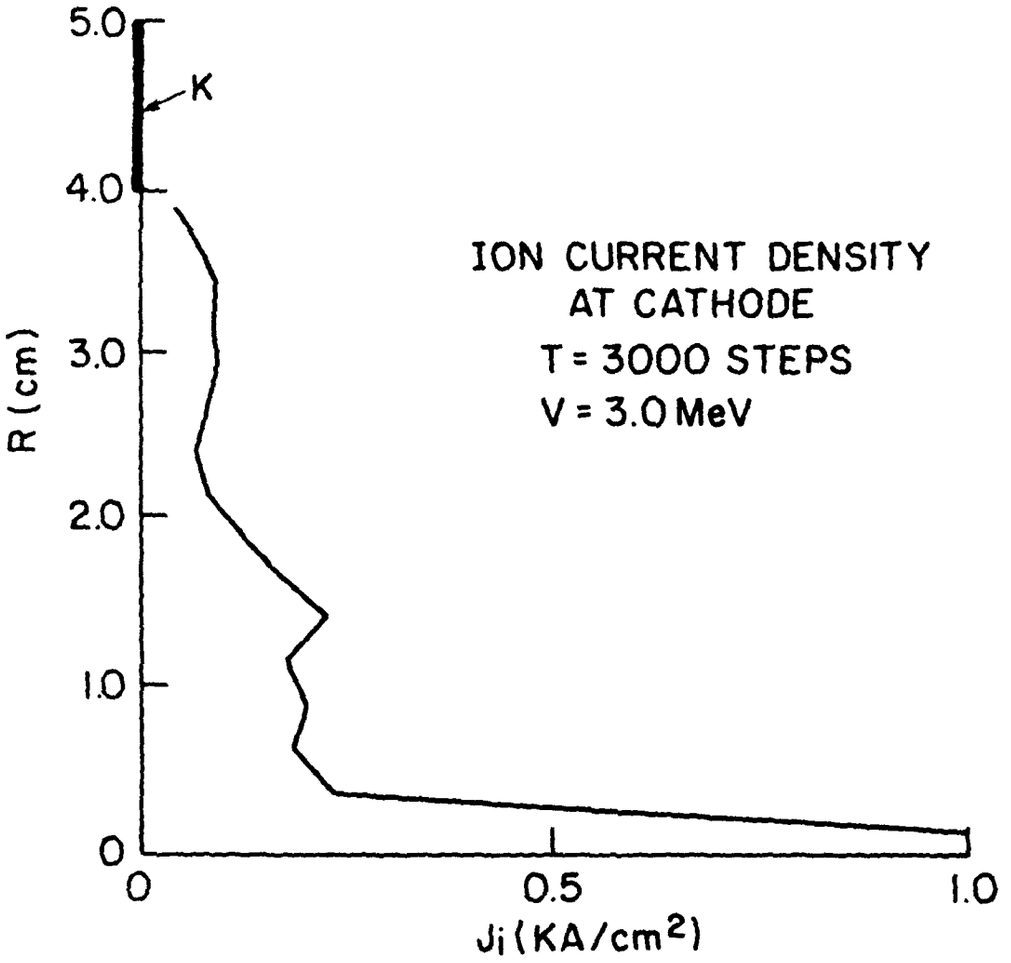

Fig. 4 — The radial profile of the ion-current density at the plane of the front surface of the cathode for the 3-MeV case

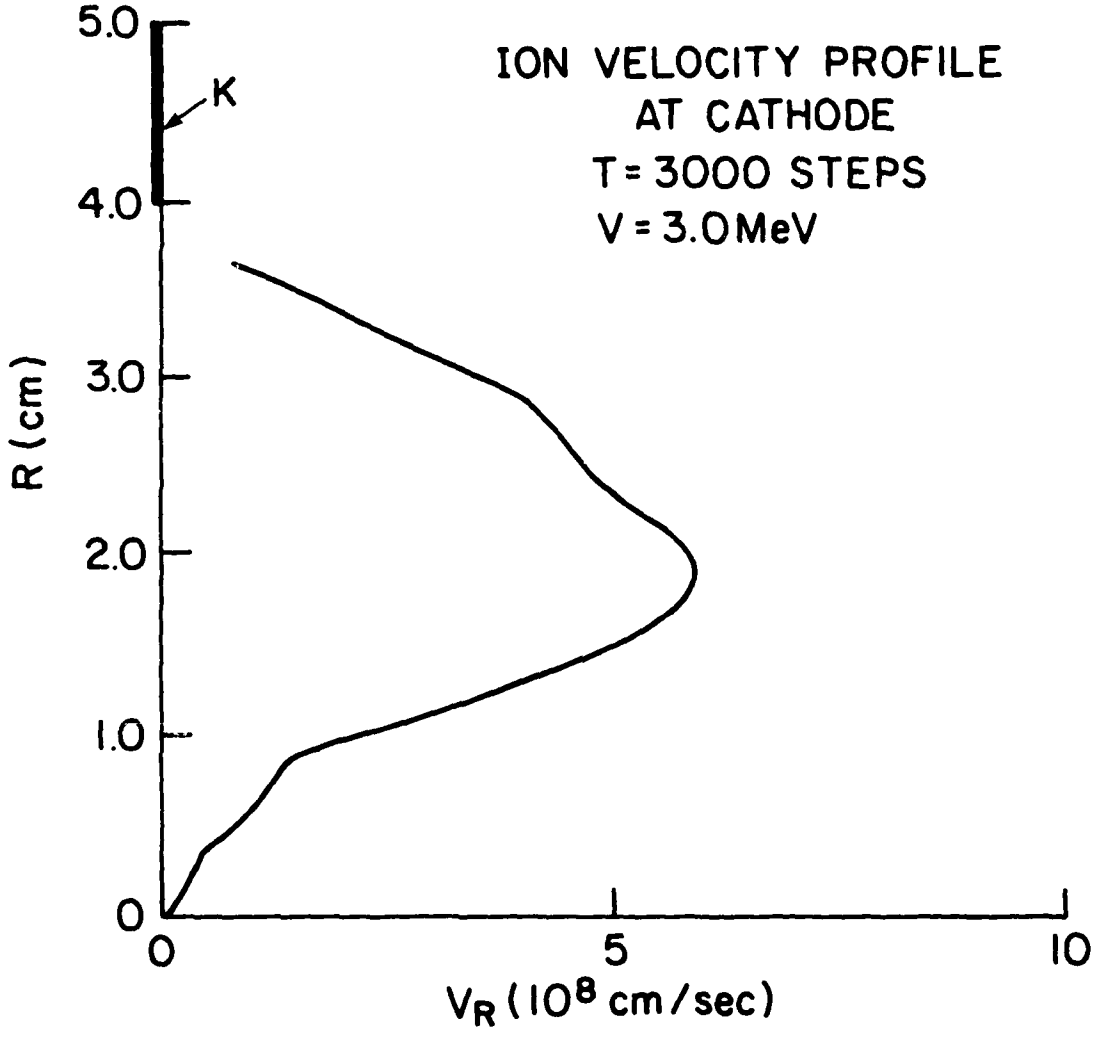

Fig. 5 — The radial velocity profile of ions at the cathode plane for the 3-MeV case

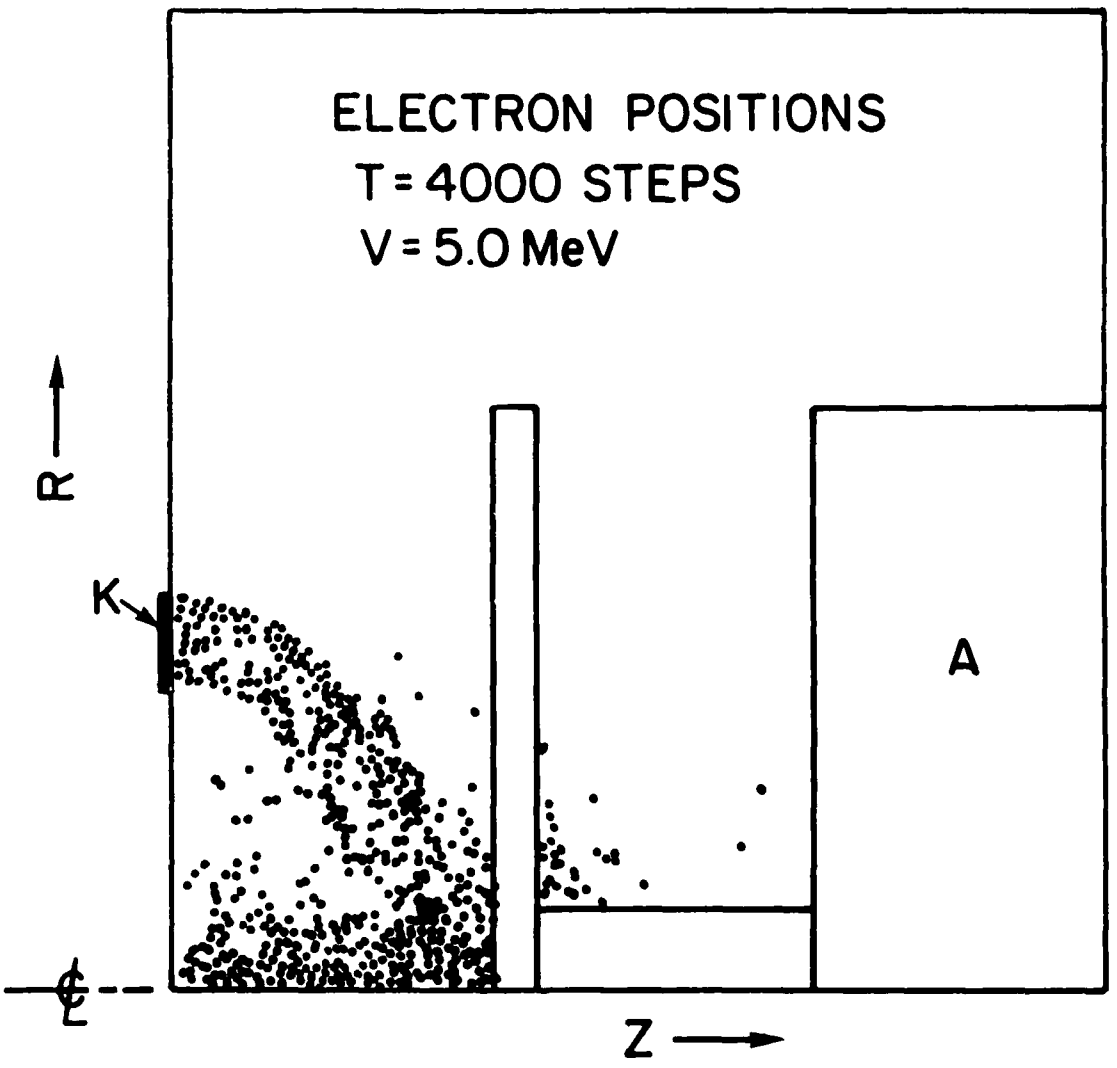

Fig. 6 — The projection of test electrons onto the (R,Z) plane for the 5-MeV case after steady state has been reached. The figure shows a focused pinch for the electrons flowing back towards the cathode plane at small radii.

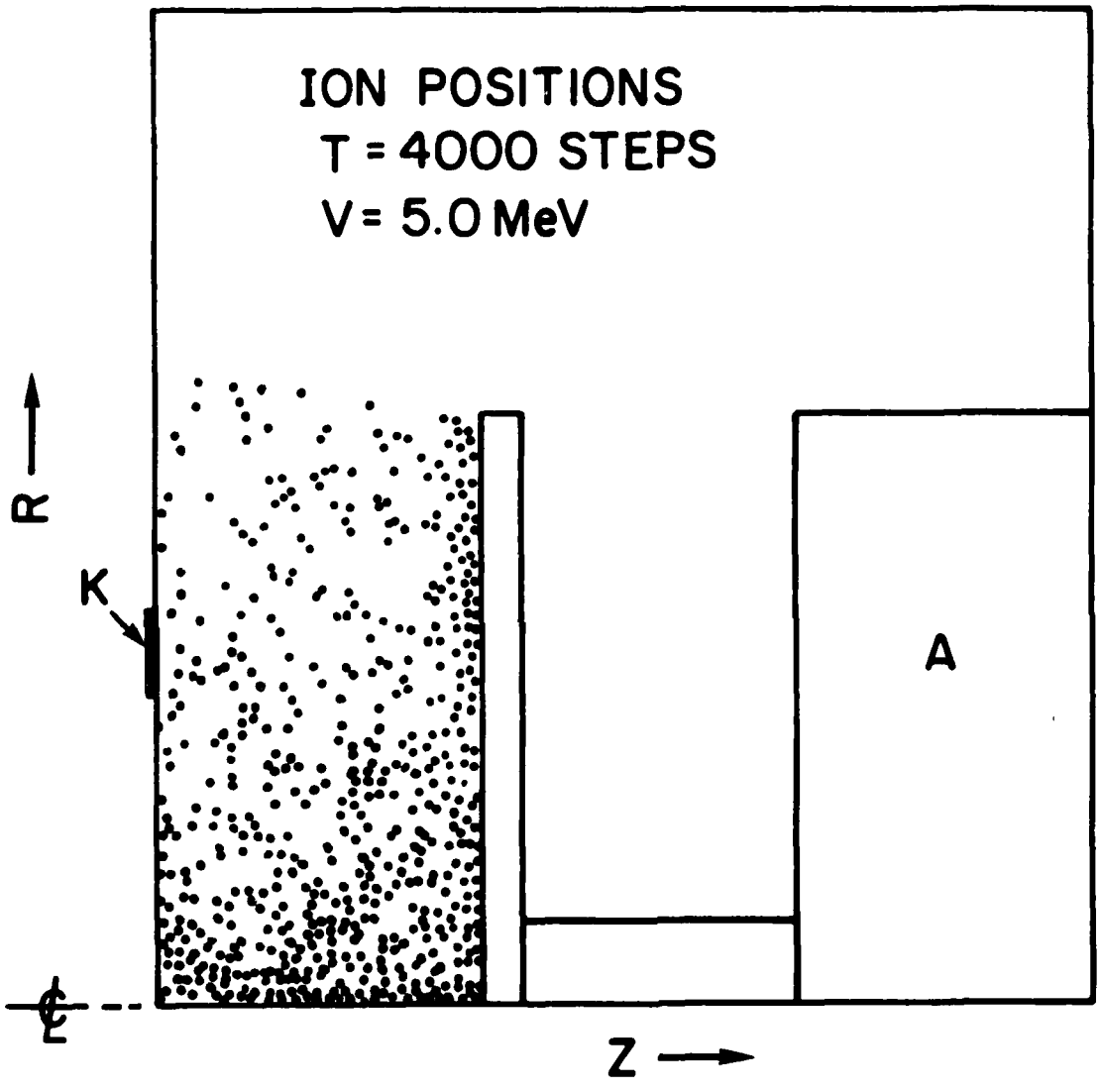

Fig. 7 — The positions of test ions projected onto the (R,Z) plane for the case shown in Fig. 6

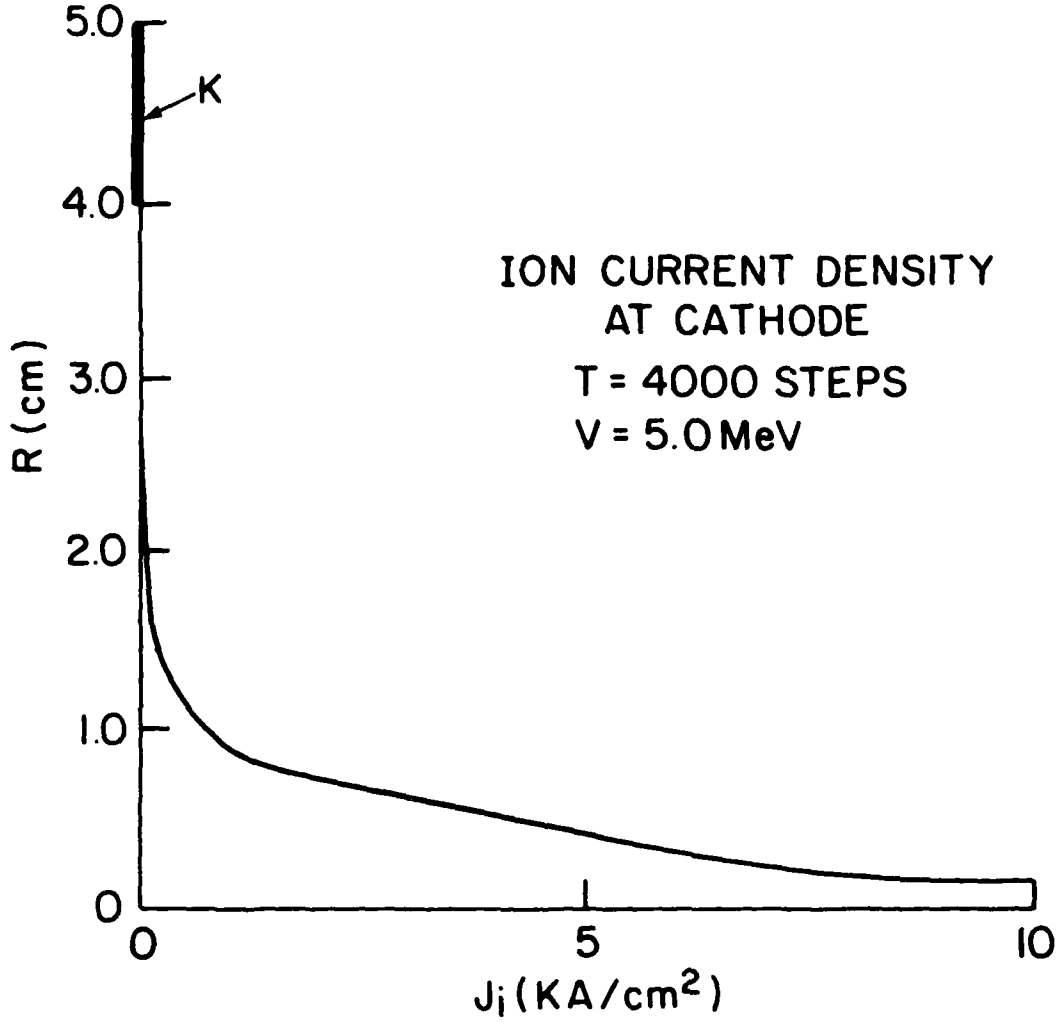

Fig. 8 — The ion-current-density profile at the cathode plane for the 5-MeV case. A strong peak on axis is observed.

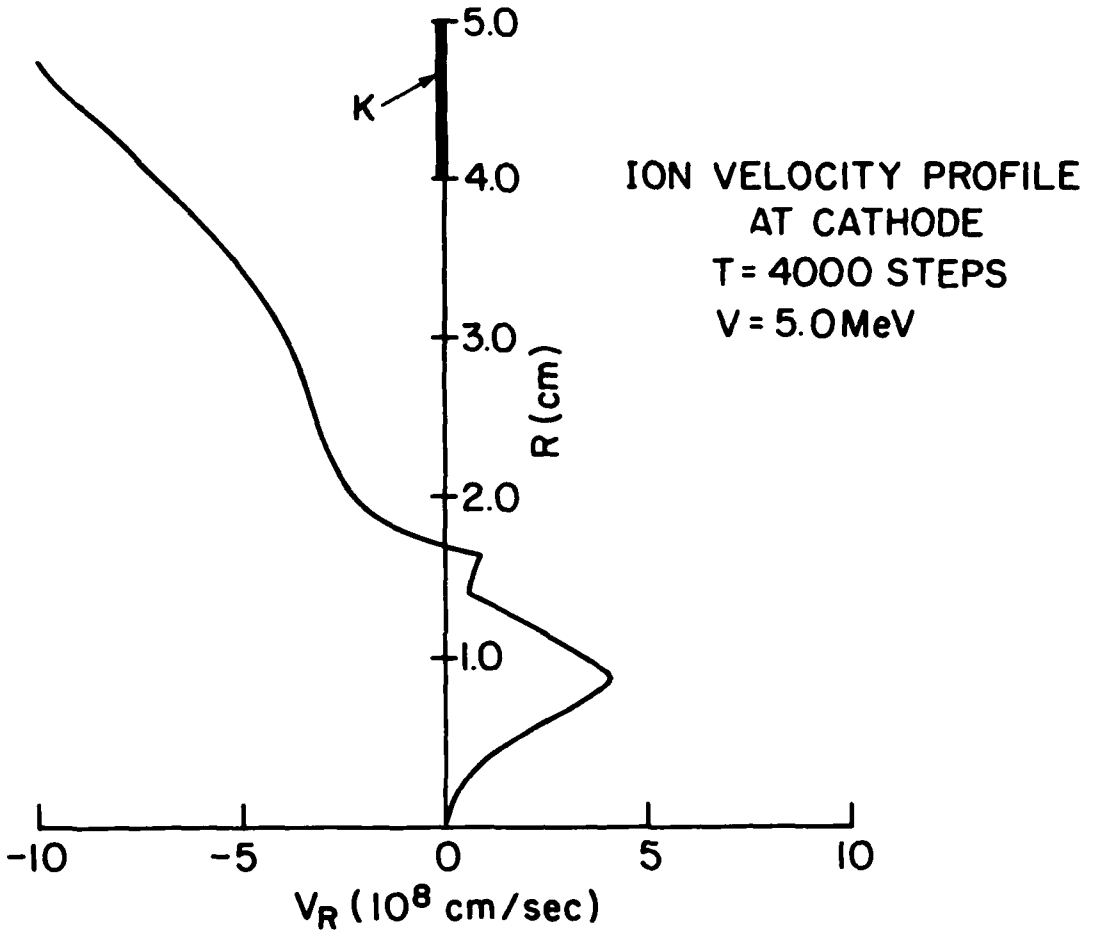

Fig. 9 — The radial velocity profile of ions at the cathode plane for the 5-MeV case. This velocity profile when compared to the 3-MeV case suggests some ion focusing is taking place in the diode. Some of the ions may even have crossed the axis.

smaller near the axis than for the 3 MeV case while the v_Z component is larger due to the higher voltage ($v_Z \sim 3.1$ cm/ns). Note also that the ion velocity goes negative for R >1.6 cm suggesting the outer ions are being focused.

The electron orbits for the 5-MeV-diode-voltage case are shown in Fig. 10. The pinching effect on the electrons can be seen clearly as well as the "figure-eight" like drift motion of the electrons toward the anode. Such electron motion is characteristic of the ∇B drift of primary electrons in this diode.

III. EXPERIMENTAL PROCEDURE

I. Experimental Hardware

The Aurora Simulator has been described in detail elsewhere.[9] In this experiment, a single arm of the accelerator was used with a second elbow and extension section in place to bring the beam out in the horizontal plane.[8] The Marx generator was operated in negative polarity at the 90-kV charge level, well below the maximum 120-kV charge available. The Marx charges a Blumlein pulse-forming line which is discharged through an oil prepulse switch onto the diode insulator oil-vacuum interface. The pulse is transmitted through a 10-meter long, magnetically-insulated coaxial transmission line to the ion diode. The geometric impedance of the nominal 1.2-m O.D., 0.53-m I.D. transmission line is 50 Ω. Figure 11 shows the location of voltage and current probes along the transmission line. A single resistive-divider voltage monitor was located in the oil, and three capacitive dividers were located along the line. Current measurements were made with three 7-mΩ resistive current monitors spaced along the outer coax. The resistive voltage monitor measured a peak of 10 to 11 MV for a 90-kV Marx charge while the capacitive voltage monitor (V_B) and current shunt (I_T) measured $\sim$ 6 MV and $\sim$ 190 kA, respectively. These values suggest that

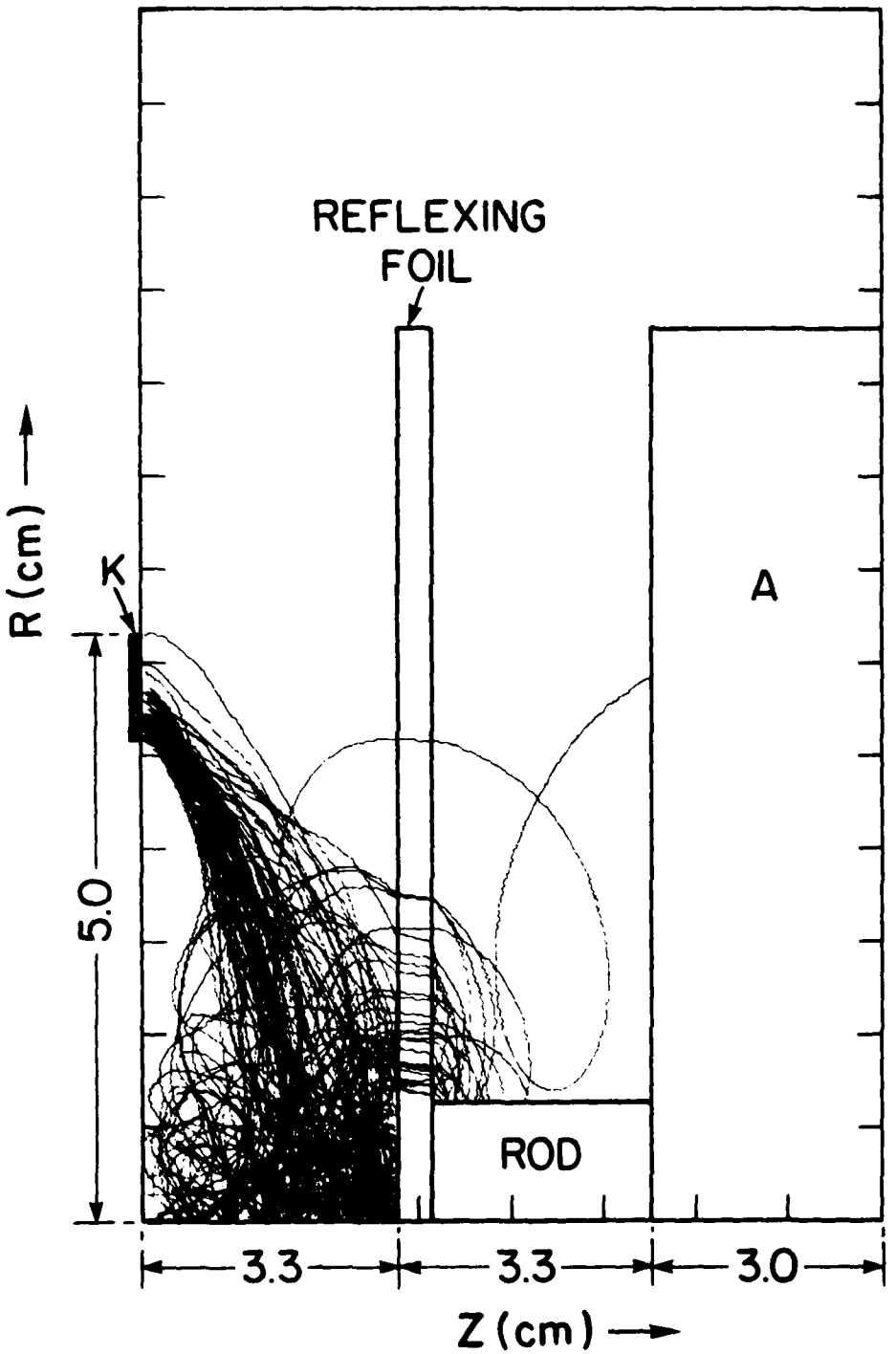

Fig. 10 — Test electron orbits for the 5-MeV case showing the complicated trajectories that are responsible for the enhanced electron lifetime. The orbits are projected onto the (R,Z) plane.

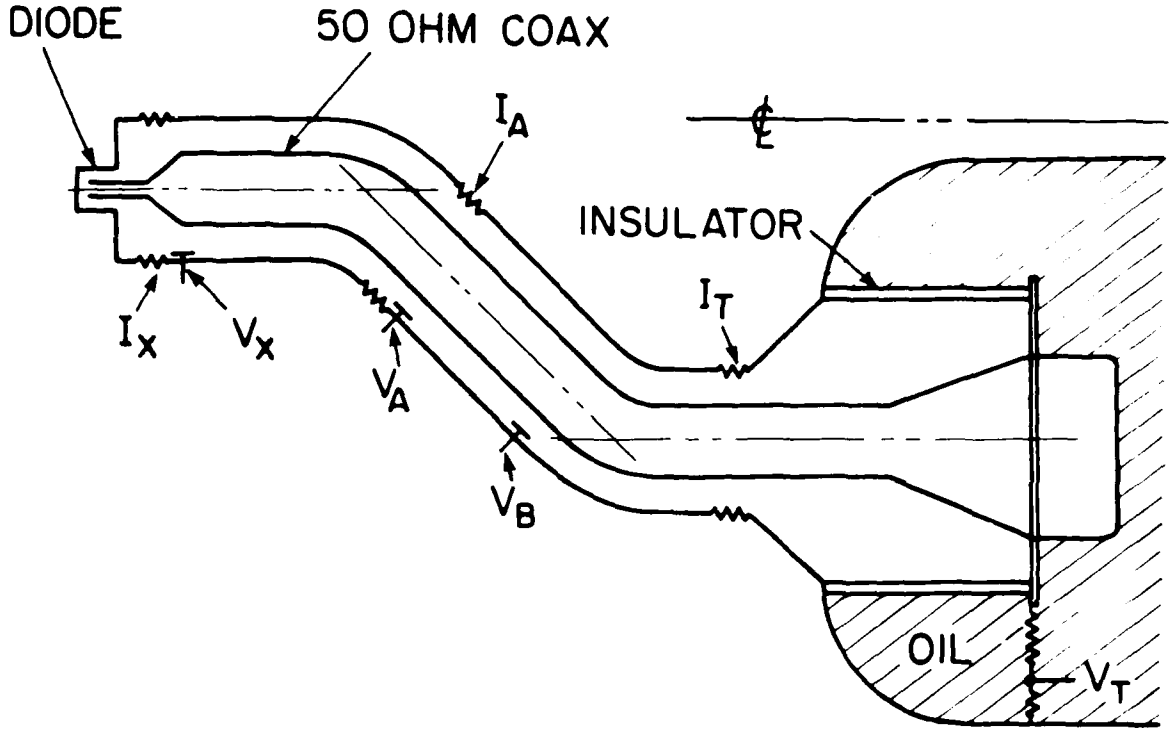

Fig. 11 — One arm of the Aurora accelerator from the oil region to the ion diode. The resistive voltage divider in the oil is shown as well as various resistive current shunts and capacitive voltage monitors in the vacuum coax.

the diode was operating somewhat below the geometric 50-Ω impedance. A prepulse of 150-200 kV peak and ~ 300 ns FWHM was measured on the vacuum coax 1.5 μsec before the main pulse.

An enlarged view of the ion diode end of the coaxial transmission line is shown in Fig. 12. The 53-cm diameter center stalk tapers to 10 cm while still in the 1.2-m diameter chamber. After a 50-cm long section, the outer conductor is reduced to 25 cm to recover the 50-Ω line impedance. A prepulse switch is located on the center stalk just downstream of the large-diameter transition as shown in Fig. 12. The switch consists of a series of acrylic insulators and field grading rings. The insulator was designed to capacitively divide the prepulse down below 50 kV depending on the number of insulators in place. The cathode was mounted on the 10-cm diameter inner stalk and was aligned with the anode mounted on an aluminum plate in the 25-cm I.D. vacuum region. A 35-cm long vacuum chamber with a carbon beam dump was located downstream of the anode.

The cathode and anode used in these experiments are illustrated in Fig. 13. The cathode consisted of a 10-cm diameter, 6-mm thick wall aluminum tube with a rounded edge. An aluminum witness plate was recessed inside the cathode. On most shots, lithium chloride (LiCl) was deposited on the witness plate to provide a neutron source through the $^{7}Li(p,n)^{7}Be$ reaction. The anode consisted of 100-μm thick polyethylene (CH_2) foil stretched between a 0.8-mm thick, 15-cm diameter aluminum ring and a 2.5-cm diameter central aluminum disk. The outer edge of the center disk and the inner edge of the ring were sharp to enhance surface breakdown of the CH_2 foil. The center disk was covered with various thicknesses of CH_2. An aluminum round-head screw clamped the anode onto a 1.9-cm diameter, 0.17-mm thick, 6-cm long aluminum tube. The entire anode was bolted onto a 1.5-mm

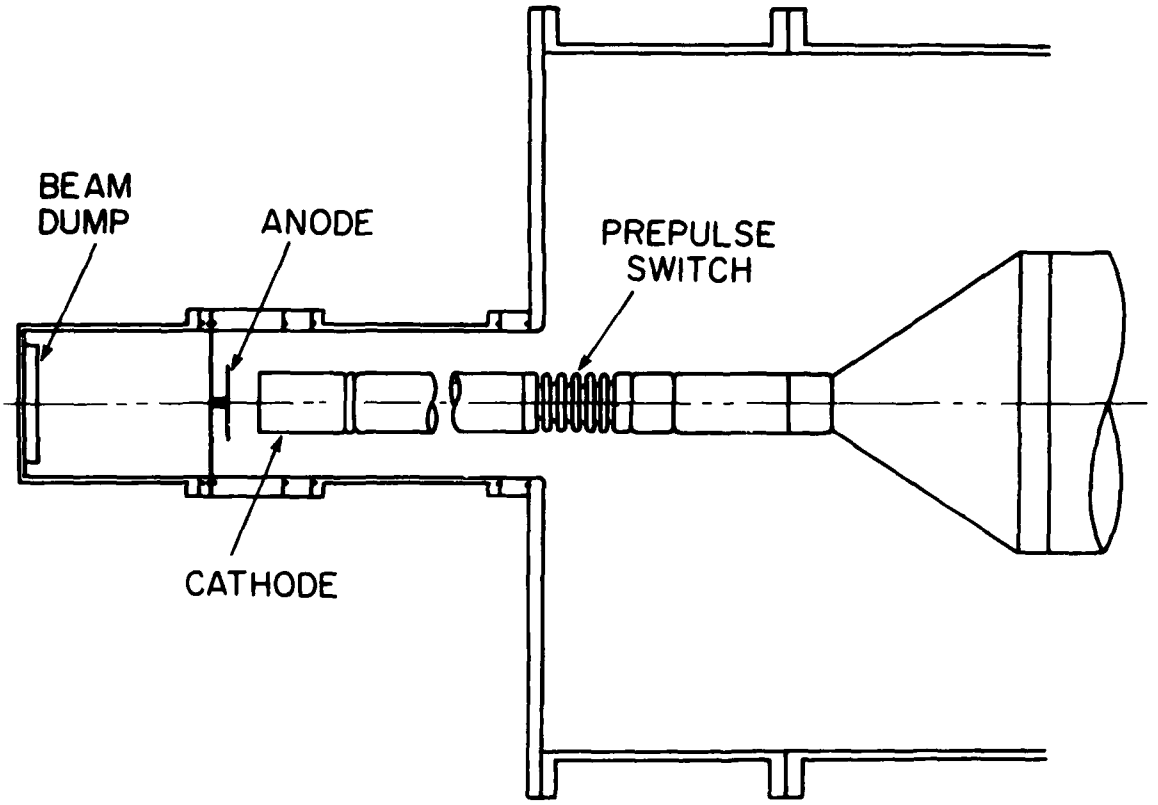

Fig. 12 — The diode end of the vacuum coax as used in the ion-diode experiments

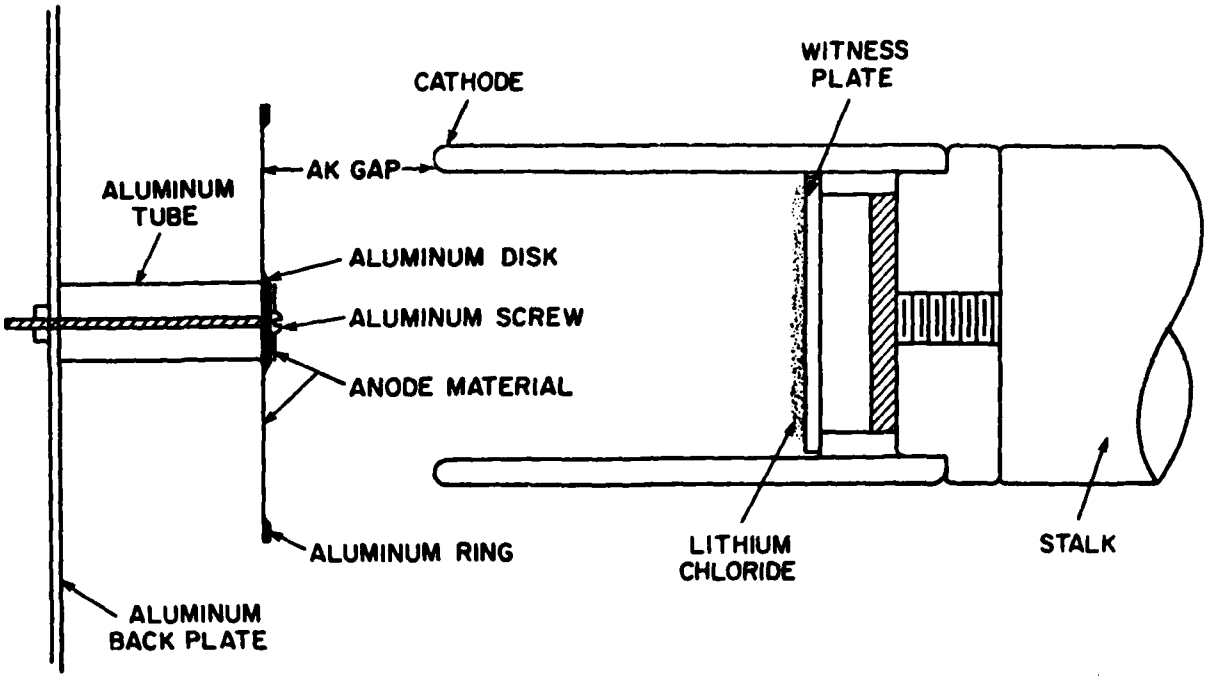

Fig. 13 — Details of the cathode and anode used in the negative-polarity, ion-diode experiments

thick aluminum plate. The anode structure was made of thin aluminum to limit debris from the shot as well as to allow many reflexes of electrons through the structure (the range of 5-MeV electrons in aluminum is 1.1 cm).

2. Diagnostics

a. X-Ray

X-ray and neutron diagnostics used in this experiment are indicated schematically in Fig. 14. Because the machine was operated in negative polarity and there was no access to the center stalk, all ion diagnostics were, of necessity, remote or delayed. X-ray diagnostics consisted of a collimated photodiode and a pinhole camera, both directed at the diode region, and TLD's placed at various locations to provide gross x-ray fluxes. The pinhole camera had a demagnification factor of 1/3.5.

b. Neutron Time of Flight

The neutron time-of-flight (TOF) technique was used to determine the proton energy in the diode. The TOF detector consisted of a 6.7-cm diameter by 5.6-cm cylindrical plastic scintillator coupled to a photomultiplier tube and mounted within a 7.6-cm thick lead shield. This detector was deployed at 10^{o} to the anode-to-cathode axis and at 13.8 m from the LiCl target. At this angle the proton energy for the $^{7}Li(p,n)^{7}Be$ reaction is a sensitive function of the neutron energy as shown in Fig. 15. Also, in this figure is shown the dependence of proton energy on neutron flight time, which is the quantity directly measured by the TOF technique. The neutron energies are small enough so that the TOF signal is well separated from the bremsstrahlung signal. For 5-MeV protons, the neutron energy is about 3 MeV and the flight time is $\sim$ 0.5 μsec. The bremsstrahlung

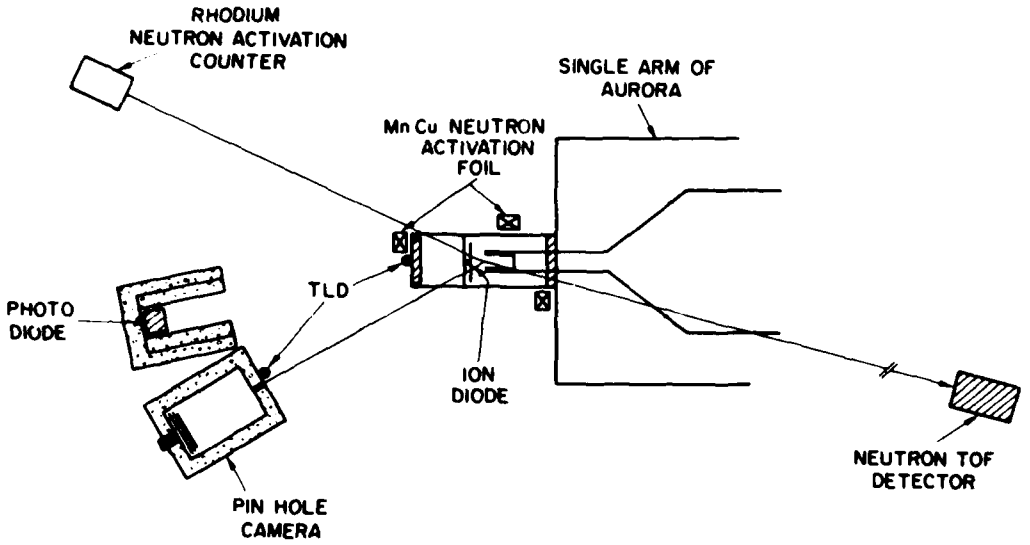

Fig. 14 — A schematic arrangement of the x-ray and neutron diagnostics

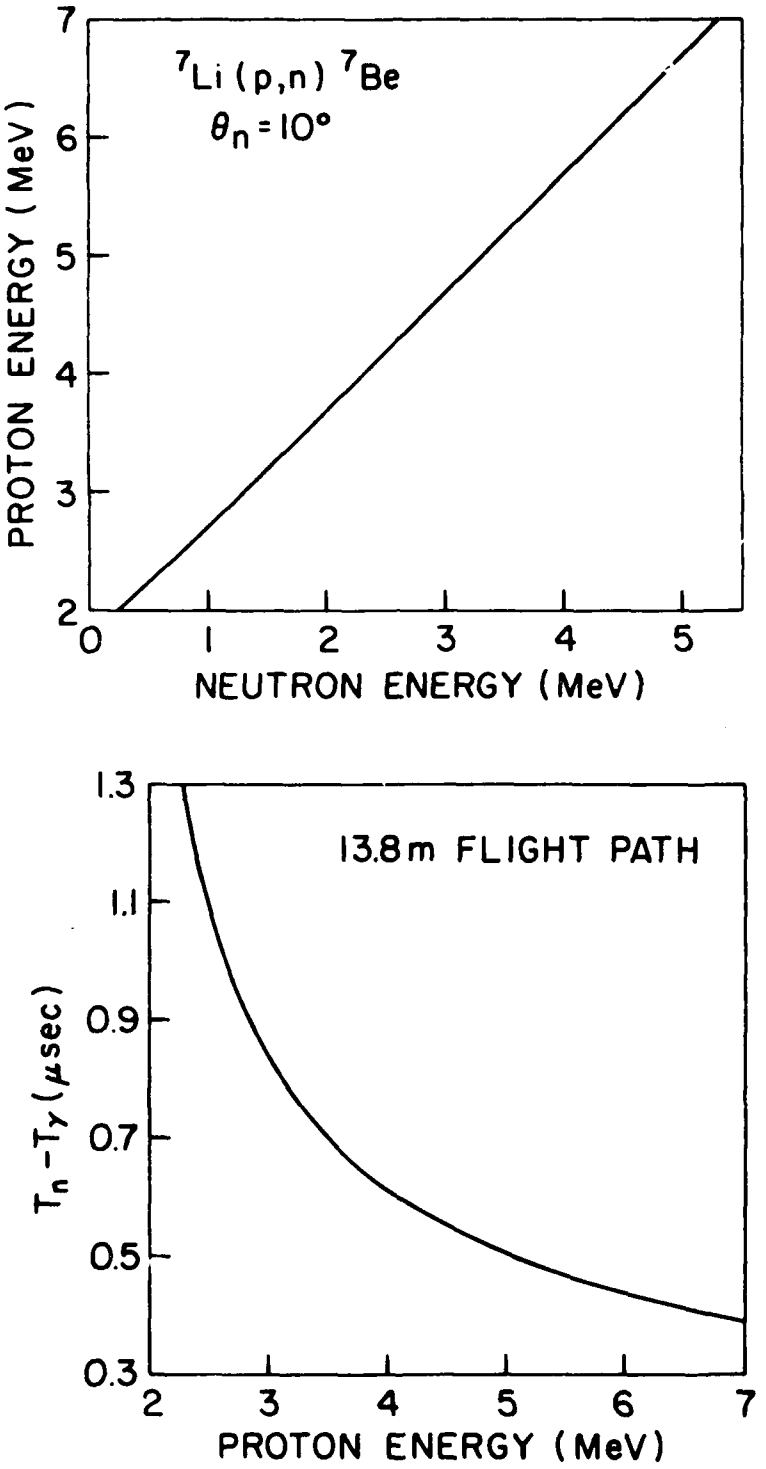

Fig. 15 — The dependence of the energy of protons in the ^{7}Li(p,n)^{7}Be reaction on the energy of the outgoing neutrons and on the neutron flight time (T_n) for a neutron TOF detector at 10° and 13.8 meters. The x-ray flight time (T_γ) has been subtracted from the neutron flight time.

acts as a time marker on the TOF traces, and its flight time, T_γ, has been subtracted from the neutron flight time.

c. Shadowbox

The trajectories of ions emitted from the diode were diagnosed by measurements with a pinhole shadowbox placed within the cathode.[1] The shadowbox is illustrated in Fig. 16. It consists of a 6-mm thick stainless-steel plate which contains an array of countersunk holes and is mounted 2.6 cm in front of a polished aluminum witness plate. The stainless steel plate is masked by a thin aluminum disk which has a matching array of 1-mm diameter apertures. The aluminum witness plate will melt if >100 A/cm^2 of 5-MeV protons are deposited, and it will vaporize for >1.4 kA/cm^2. The front aperture plate was coated with LiCl for neutron diagnostics.

d. Cathode Activations

Measurements of residual radioactivity on the cathode were made after each shot to provide additional information about the ion beam. The γ-ray activity of the cathode stalk was measured with a cylindrical 7.6-cm diameter by 7.6-cm NaI detector. Counting of the cathode could be initiated 15 minutes after a shot. Pulse-height spectroscopy was used to determine γ-rays due to radioactive species produced by ion bombardment of the cathode.

e. Neutron Activation Techniques

Neutron intensities were determined with a Rh-activation detector[10] and an array of Mn-activation foils. The Rh detector was deployed at 155° to the ion-beam direction, and Mn-foil samples were positioned at several different angles as noted in Fig. 14. The Rh-detector consisted of a 5-cm diameter Rh-foil mounted against a plastic scintillator and enclosed in a polyethylene moderator.[11] Due to the intense neutron yields in this

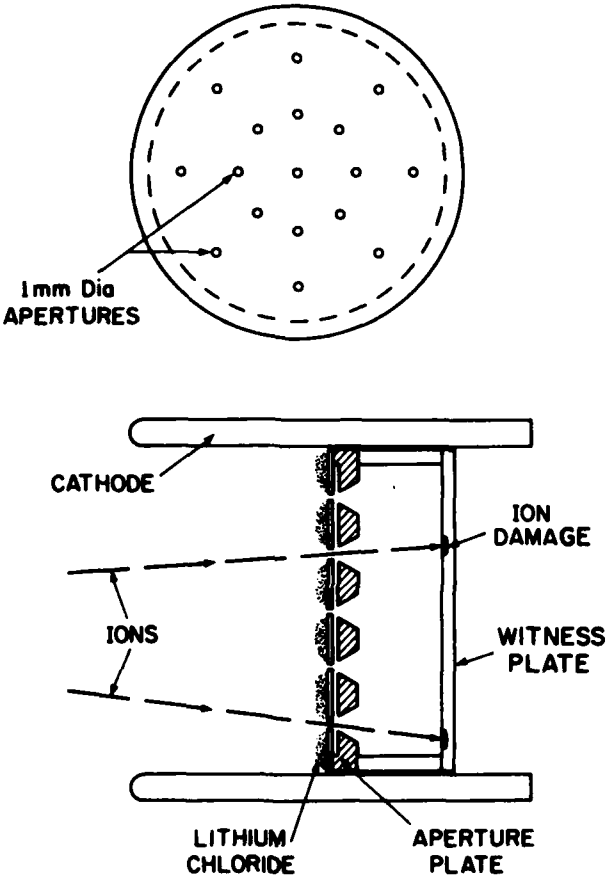

Fig. 16 — A schematic of the shadowbox used in these experiments. The aluminum mask with 1-mm diameter apertures allows LiCl to be deposited on its front surface for neutron diagnostics while protecting the stainless steel aperture plate. Ion damage is observed on the aluminum witness plate.

experiment a foil thickness of only 25 μm was used in this detector. Even so, it was necessary to locate this detector several meters from the LiCl target to prevent pileup effects.

Measurements with Mn-foil activations were used to provide neutron intensities at different angles and distances from the target on a single shot. This activation technique is illustrated in Fig. 17. Foils of Mn-Cu (81% Mn) 2.5 cm in diameter and 50-μm thick were placed in the center of a cylindrical 7.6-cm diameter by 7.6-cm CH_2 moderator. After this assembly was exposed to neutrons on a shot, the Mn foil was removed and its activity was measured with a cylindrical 7.6-cm diameter by 7.6-cm NaI detector. A γ-ray pulse-height spectrum of the induced activity is presented in Fig. 17. Gamma rays of 0.847, 1.81 and 2.11 MeV are observed. The higher-energy gamma lines (2.66 MeV and 2.96 MeV) result from summing of lower energy γ-lines. To simplify the measurement, the output count of an integral discriminator located just below the 0.847-MeV γ-ray peak was used to measure the activity. This activity decays with a 156-min half-life, as shown in Fig. 17. The combination of measured γ-ray energies and half-life is consistent with the ^{56}Mn activity expected from neutron activation via the $^{55}Mn(n,\gamma)^{56}Mn$ reaction. This measurement technique is 10^3 less sensitive than the Rh-activation detector.

Absolute calibration of these neutron detectors is based upon a calibration of the Rh counter with a Cf-252 neutron source. Calibrations with similar neutron sources have been described previously.[10] This source was used because its neutron energies are similar to those expected from the $^{7}Li(p,n)^{7}Be$ reaction. Even so, the neutron moderator on these detectors makes their response relatively insensitive to the neutron energy. For this

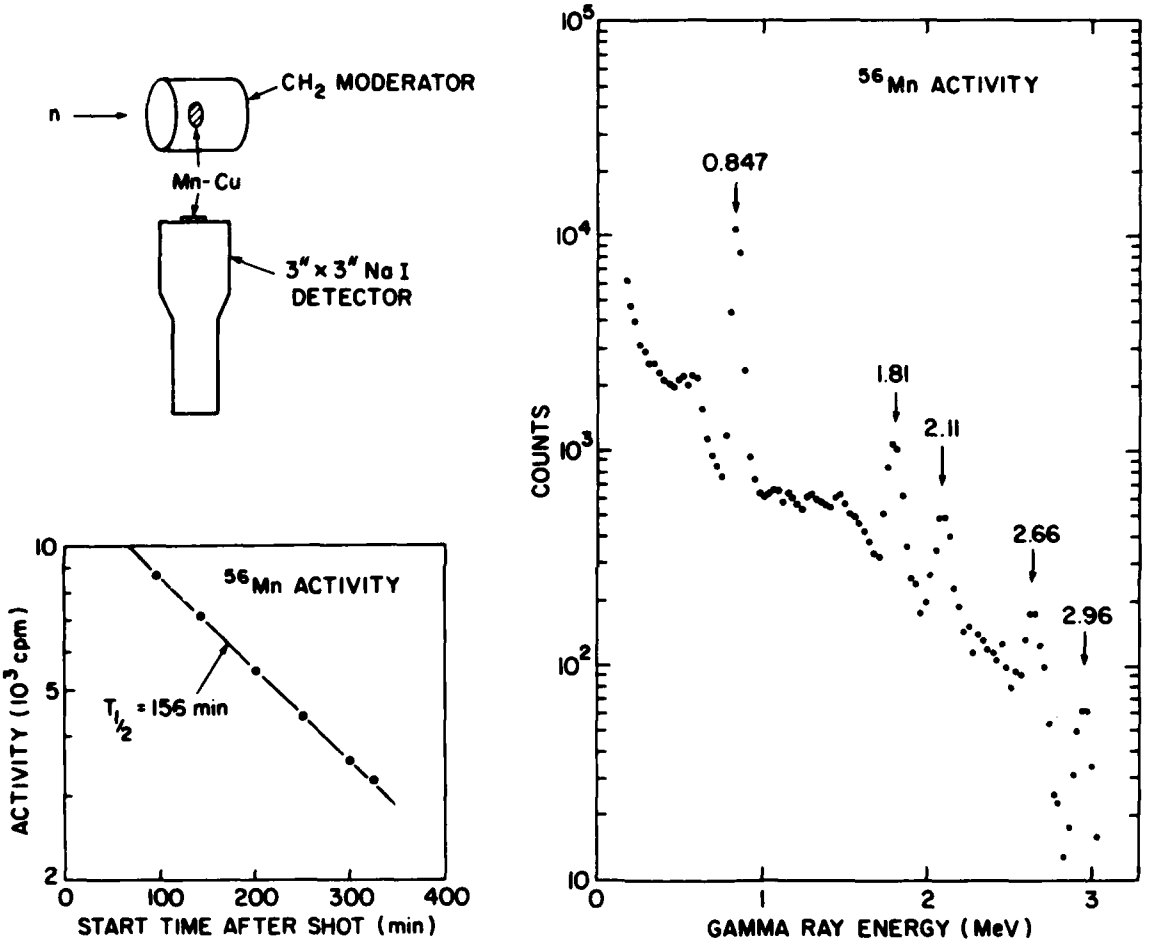

Fig. 17 — Neutron intensity determinations by Mn-foil activations. The apparatus for activating the Mn-foil and counting them is shown on the top left. A gamma-ray spectrum of the activity induced in a Mn-foil by moderated neutrons, as measured with a NaI detector, is shown at the right. This activity decays with a 156-min half-life corresponding to ^{56}Mn as shown on the lower left.

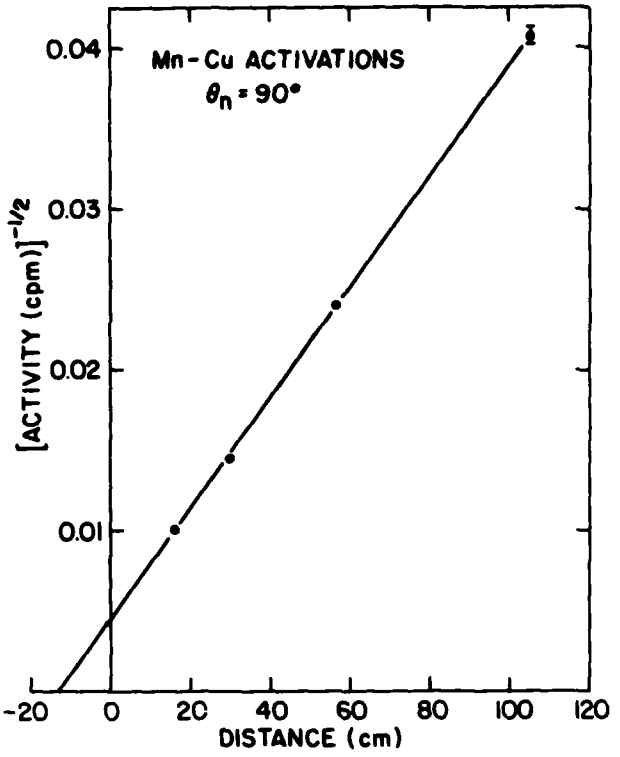

Fig. 18 — The dependence of Mn-foil activations on the distance from the LiCl target is shown for an array of four Mn-samples located at 90° from the ion beam direction in the plane of the target for a single shot. The plot demonstrates the inverse-square scaling of the neutron emission with distance out to ~ 1 meter.

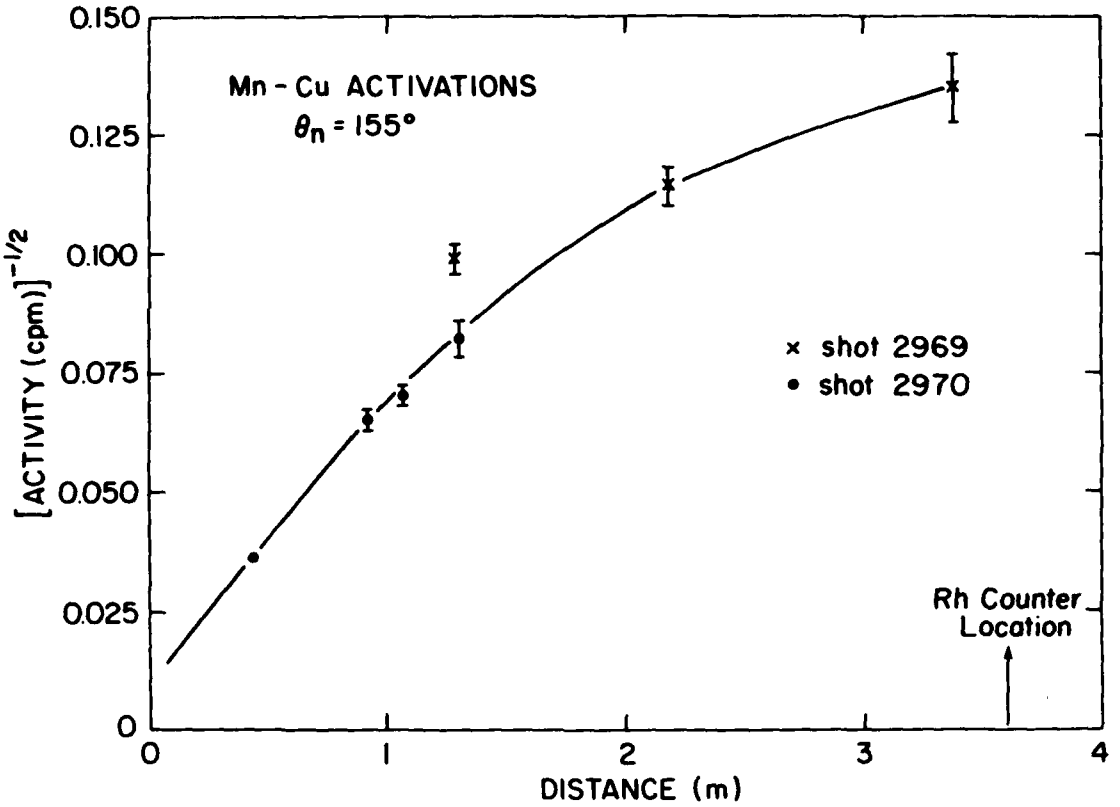

Fig. 19 — The dependence of Mn-foil activations on the distance from the LiCl target to the Rh-counter. The nonlinearity indicates that inverse-square scaling with distance is not obeyed for distances greater than one meter.

calibration, the detector response was observed to scale inversely with the square of the distance. The calibration factor, F, in neutrons/sr/cpm is

$$F = \frac{83}{4\pi} (d + 6.5)^2$$

where d is the source-to-detector distance in cm. This factor was used to convert the measured activity into neutron intensity. This Rh-detector calibration is three times smaller than a previous calibration[10] of the detector with a d-d neutron source because the Rh foil is of smaller thickness.

To apply this absolute calibration to the ion diode experiments, the scaling of neutron intensity with distance from the target was determined with the Mn-activation technique. The activation of an array of four Mn-Cu samples positioned from 0.16 to 1 meter from the LiCl target is shown in Fig. 18. The samples were located at 90° to the anode-cathode axis. In this figure, the square root of initial activity induced in each foil has been plotted against the target-to-detector distance. The linearity of these data demonstrates the inverse-square scaling of the neutron emission out to a distance of one meter. Similar measurements with arrays of Mn-Cu samples positioned along the direction of the Rh counter are shown in Fig. 19 for two different shots. The activities on these shots are normalized to each other by using measurements from the Rh detector and a Mn-Cu sample at 20°. The normalizations determined by these two independent neutron monitors were in agreement within 5%. The nonlinearity of the data in Fig. 19 indicates that the neutron intensity no longer obeys inverse-square scaling at distances greater than one meter. This deviation is attributed to room scattering of neutrons. Clearly, inverse-square scaling with distance is not appropriate for the Rh-counter positioned at 3.6 meters.

In order to use the Cf-252 calibration where the neutron emission obeyed inverse-square scaling, the Rh-counter was positioned 0.76 m from the LiCl target. For each shot the Rh-counter activity was measured for several minutes to identify the two decay components expected from Rh activation. With the detector located closer to the target, pulse pileup of the detector output at early time was observed as indicated by the data points in Fig. 20. To correct for this problem, the shape of the decay curve at early time was determined from a shot where the counter was 3.6 m from the target and did not suffer pulse pileup. The solid line in Fig. 20 is such a decay which has been normalized to the late-time measured activity. Then an absolute neutron-intensity determination could be performed by combining the Cf-252 absolute calibration with the first minute count implied by the solid line in Fig. 20.

IV. EXPERIMENTAL RESULTS

1. Results from a Typical Shot

Experimental results will be presented by discussing a single shot (No. 2978) in detail. In most aspects this shot typifies all the shots for this ion-diode experiment. The Marx generator was charged to -90 KV producing a 8.3-MV peak voltage on the Blumlein before being discharged across the insulator stack and onto the vacuum coax transmission line. Figure 21 shows a plot of the tube voltage (V_T) in the oil just before the insulator stack. The peak value of 11 MV is slightly higher than the 10.3-MV average peak value for the entire run (25 shots). The voltage risetime of ~ 100 ns with ~ 150 ns FWHM is typical. Figure 21 also shows the capacitive voltage monitor signal (V_B). Its peak of 6.3 MV is typical. The 40% drop in peak voltage between V_T and V_B is consistent with computer

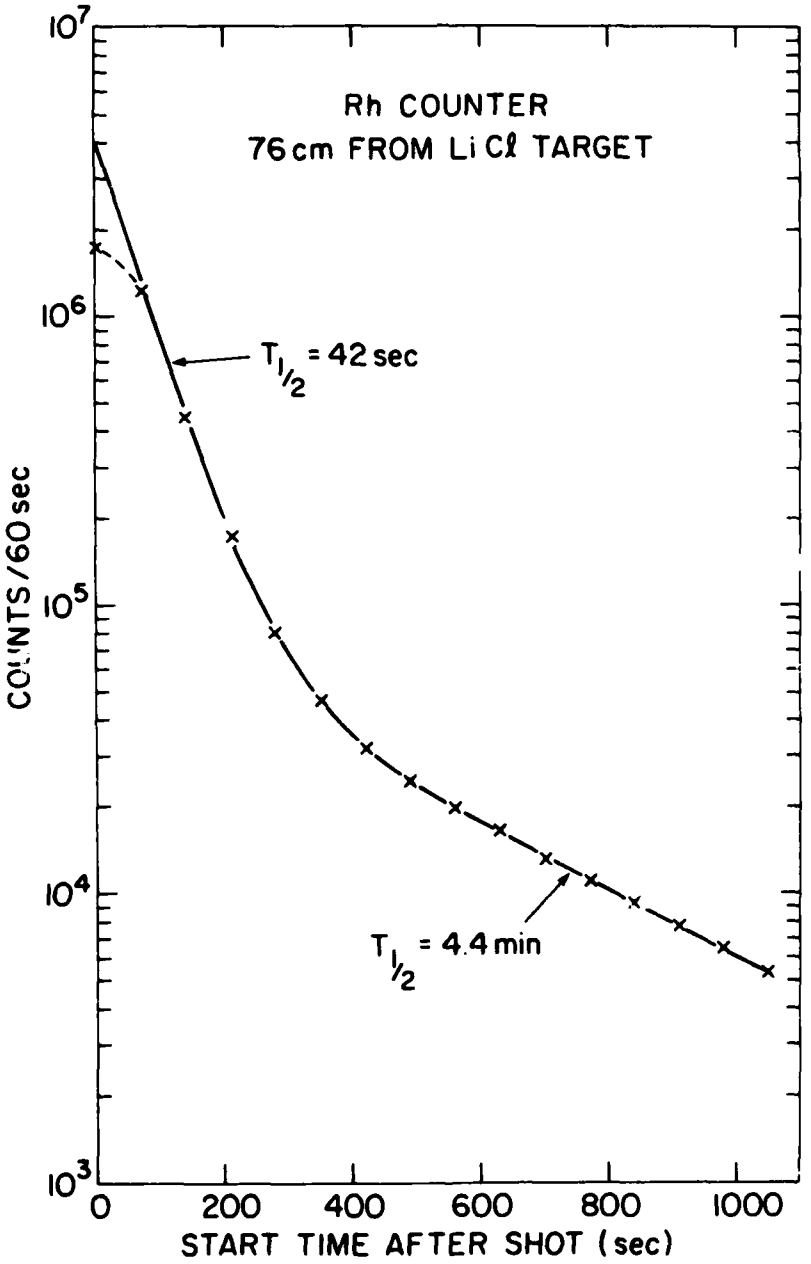

Fig. 20 — The measured decay of the activity induced in a Rh-counter by an intense burst of neutrons. The data points are for an intense pulse resulting in pulse pileup at early times. The solid line is the decay curve resulting from a less intense burst of neutrons and has been normalized to the late-time data points.

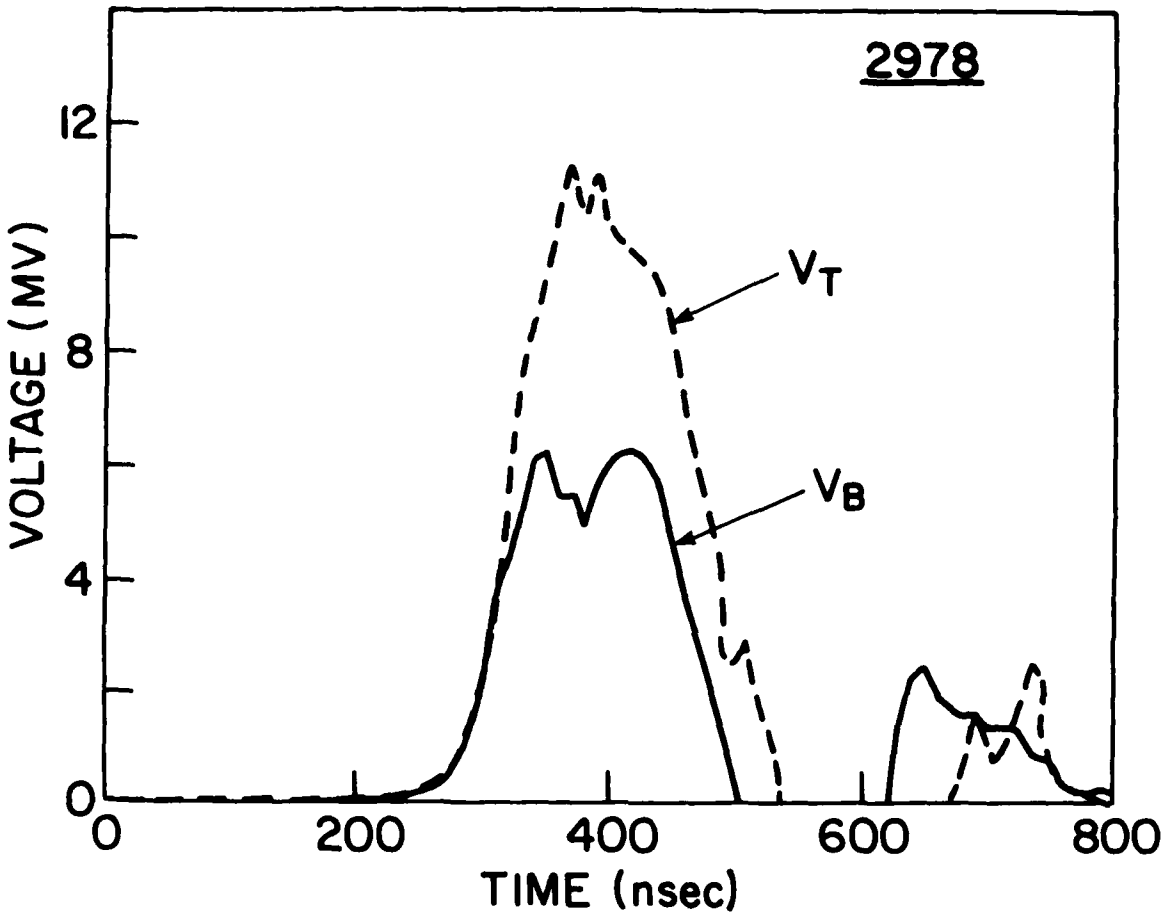

Fig. 21 — Two voltage wave shapes are shown, namely the copper sulphate voltage divider located in the oil (V_T) and a capacitive monitor located in the vacuum transmission line (V_B)

modeling of the generator and is the result of the impedance mismatch between the Blumlein and the vacuum coax. Voltages measured closer to the ion diode have wave shapes similar to V_B. No direct measurement of the cathode voltage was made. A diode voltage of ~5 MV is inferred from neutron TOF measurements to be discussed below.

Figure 22 compares the voltage, V_B, the current, I_T, just downstream of the diode insulator, and the effective line impedance $Z = V_B/I_T$. This current rises in ~120 nsec to a peak value of ~190 kA and plateaus for the remainder of the voltage pulse. The value agrees with the average peak current of 25 shots which ranges from 210 kA to 170 kA depending on the diode configuration. The calculated impedance at this location has a plateau of ~30 Ω for ~100 nsec during the useful portion of the diode pulse. Figure 23 shows the power and energy derived from V_B and I_T. The peak power of ~1.2 TW is typical for this run. At the end of the voltage pulse, these probes have measured ~160 kJ. The diode voltage will be lower than V_B and the diode current higher than I_T due to the impedance mismatch between the transmission line and the ion diode. Transmission line computer code studies[12] indicate that the current is ~250 kA in the diode region. This result coupled with the ~5-MV diode voltage implied from the TOF measurements suggests that the diode was operating close to 20-Ω impedance.

The ion diode used on this shot had a 4.9-cm anode-cathode (AK) gap. The anode consisted of a 86-μm thick CH_2 foil on the outer section and a 0.43-mm thick CH_2 foil on top of the center field-enhancing disk and aluminum screw head. This anode was supported by a 6.0-cm long stalk mounted on a 1.5-mm thick aluminum diaphragm. A shadowbox was recessed

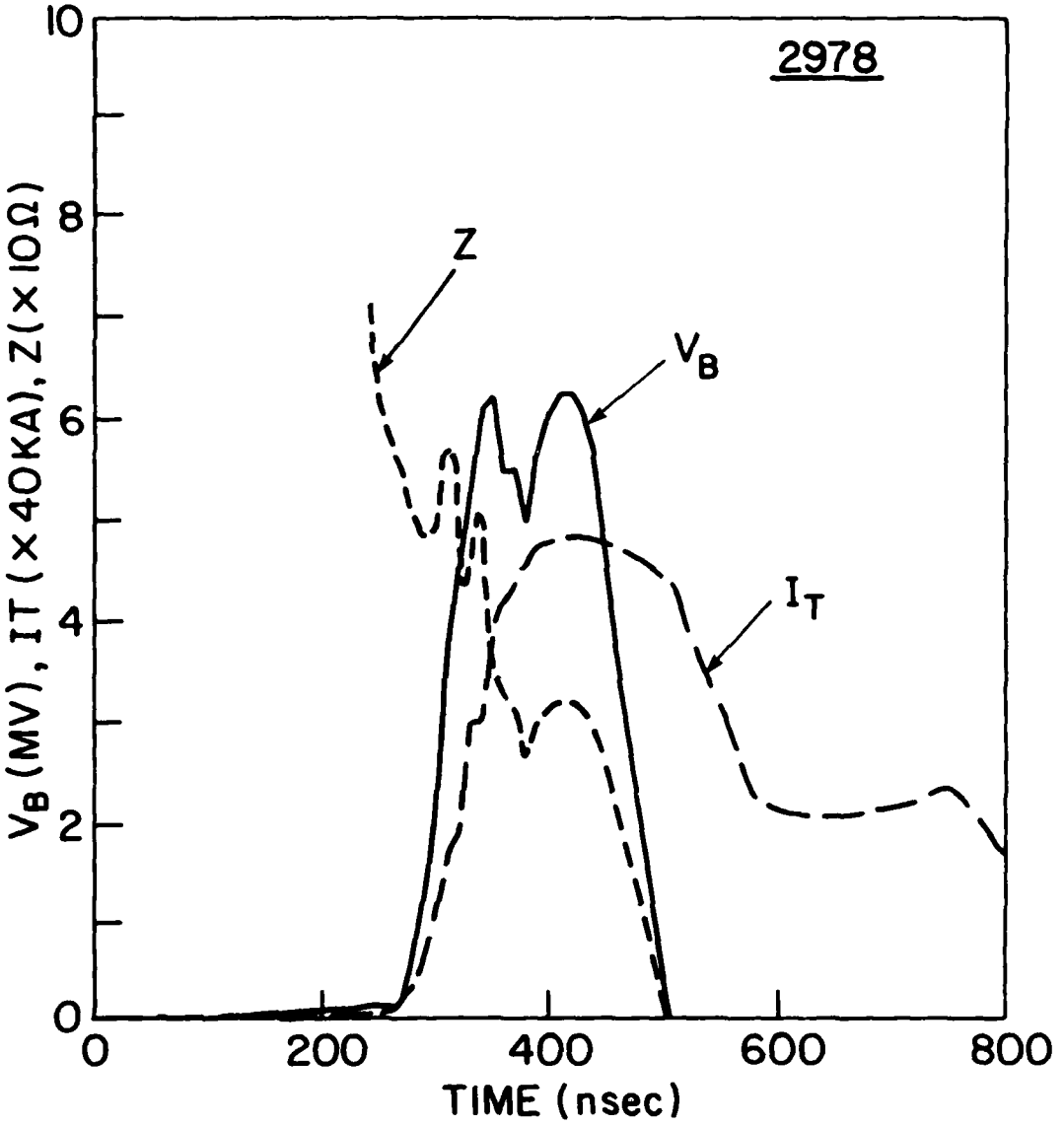

Fig. 22 — The voltage on the vacuum transmission line, V_B, is shown relative to the current I_T. The effective impedance, Z, computed from V_B and I_T is also shown. This impedance represents the combination of the vacuum transmission line downstream of the monitors and the actual ion-diode load impedance. *The line impedance appears to be ~ 30 ohms during the latter half of the pulse when the diode is fully turned on.*

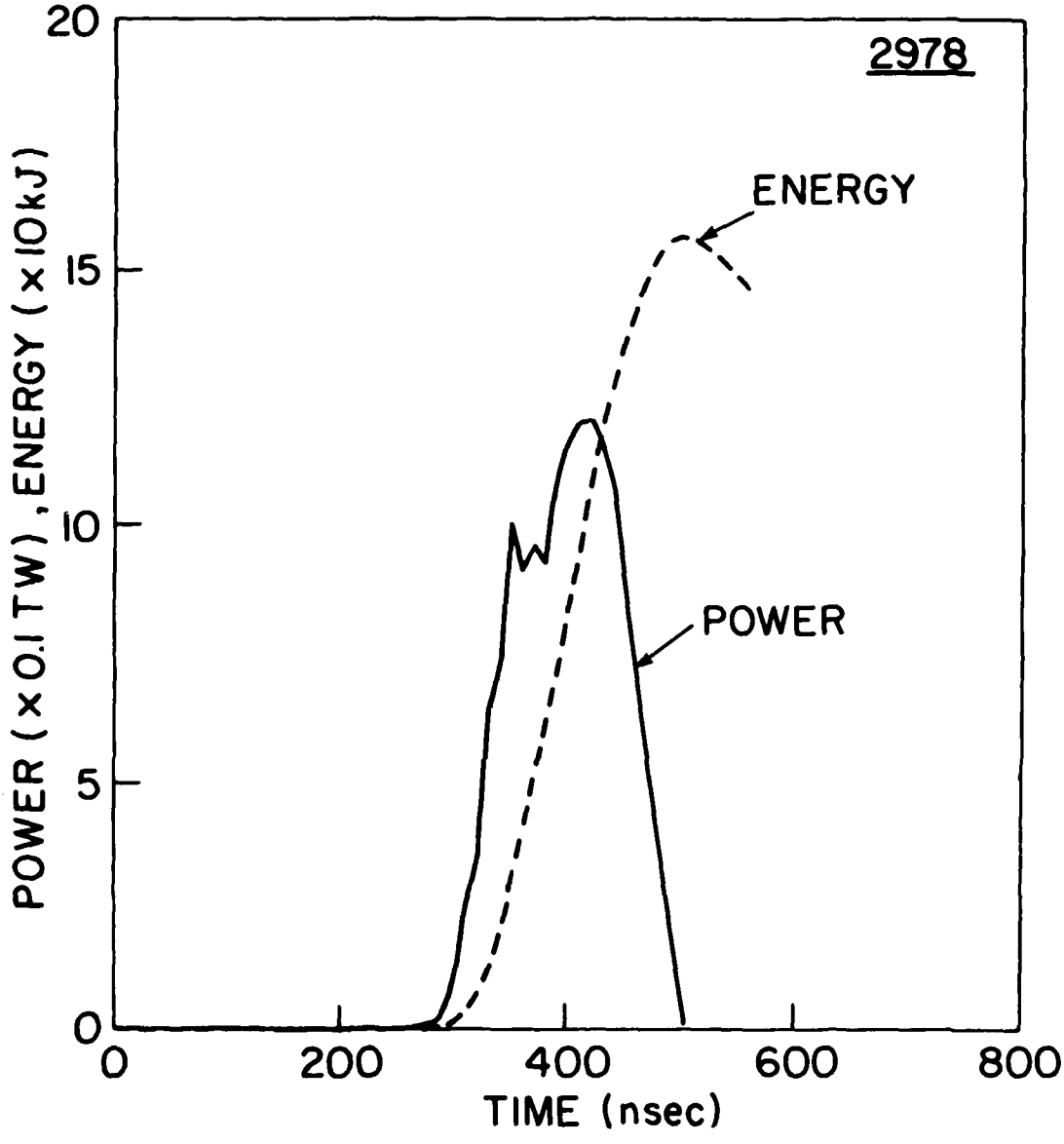

Fig. 23 — The power and energy delivered to the transmission line at the location corresponding to probes V_B and I_T as calculated using these traces

10.5 cm inside the cylindrical aluminum cathode and had a LiCl target mounted on its front surface. A four-insulator-section prepulse switch was located behind the cathode.

The results of x-ray measurements with the pinhole camera are shown in Fig. 24. Images were recorded with four different film sensitivities through a 1.9-mm diameter pinhole. These pictures are typical of the experiment. The pinch was well centered on all shots, seemingly striking the central disk or screw head. The intensity of the x-ray images depended on the diode impedance with lower impedance shots showing weaker images. In no case were bright regions observed from the aluminum back plate except near the center.

The signal measured by the x-ray photodiode for this shot is shown in Fig. 25. The shape of this signal is compared with a theoretical scaling[13] for x-ray production from e-beams given by $I_T(V_B)^{2.8}$. The calculated signal was normalized in magnitude and positioned in time for comparison with the measured signal. The shapes of the two signals agree reasonably well. This agreement provides an independent check on how well the measured voltage and current wave shapes agree with the actual wave shapes across the diode. In general, the peak intensity from the photodiode depended on the diode configuration. Intensities observed with the x-ray pinhole camera were consistent with the intensities recorded by this photodiode.

Ion diagnostics on this shot included measurements of neutrons resulting from proton bombardment of the LiCl target, pulse-height analysis of residual gamma activity from the cathode, and a shadowbox to observe the ion trajectories. Neutron diagnostics and cathode activation analyses were used on most shots, but the shadowbox diagnostic was used on only two shots.

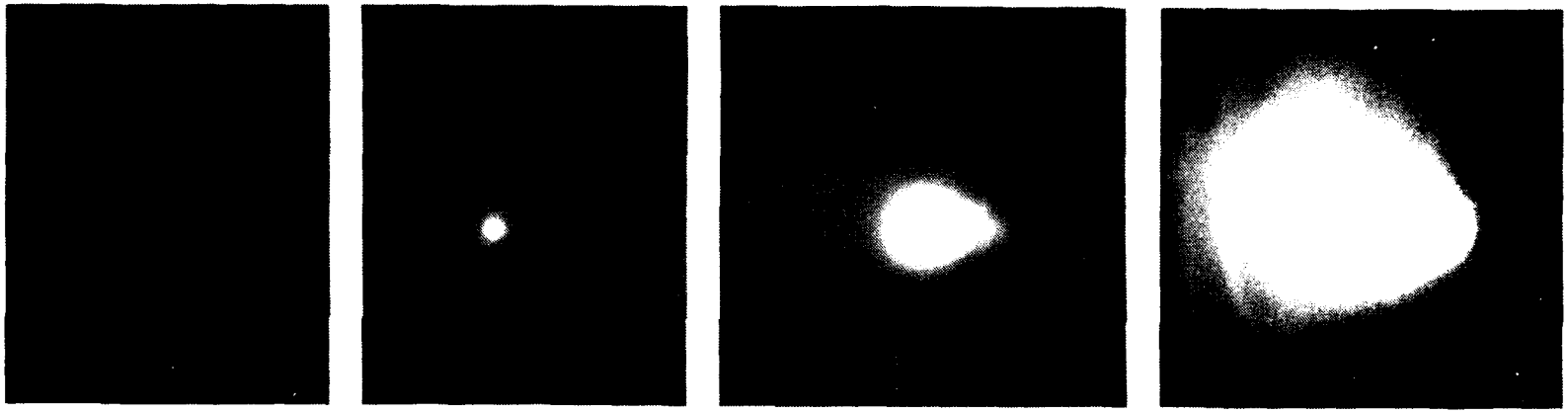

Fig. 24 — X-ray pinhole photographs at four different film sensitivities for a single shot (2978). Film sensitivity increases from left to right. On the left, only the aluminum screw head on the front of the anode (see Fig. 13) is seen. Next, some of the thin aluminum anode-supporting tube and more of the central aluminum anode disk are apparent. The outer aluminum anode ring is evident in the third image. The last image indicates that the aluminum back-plate was irradiated by a diffuse spray of electrons.

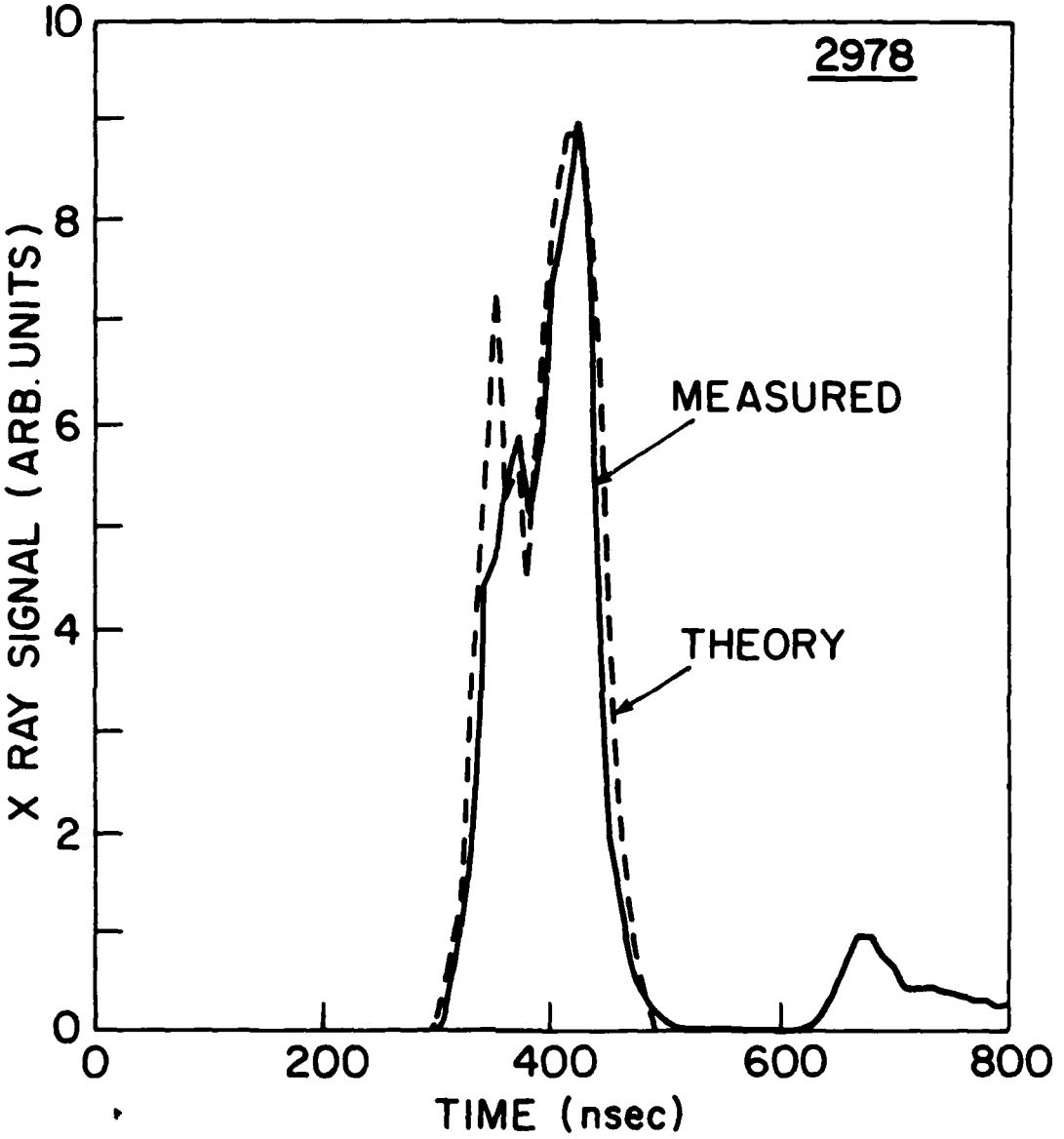

Fig. 25 — The measured signal from an x-ray photodiode collimated to see only the anode-cathode region. The dashed line represents the calculated x-ray production with the $I_T(V_B)^{2.8}$ scaling and has been normalized to the peak of the measured signal.

Neutron TOF measurements for this shot and for a shot without a LiCl target are compared in Fig. 26. The neutron pulse is readily detected above the bremsstrahlung tail. The onset of the neutron pulse is ~ 400 nsec after the peak of the bremsstrahlung and the ~ 150 nsec risetime followed by a rounded peak and long tail is characteristic of the neutron TOF data. The width of this pulse is due primarily to the duration of proton emission from the diode and the energy loss of protons in the thick LiCl target. Proton energies were extracted in two ways. First, the time interval from the peak of the x-ray pulse to the peak of the neutron pulse gives a measure of the average proton energy. Second, the time interval from the peak of the x-ray pulse to the 50% point on the leading edge of the neutron pulse gives an estimate of the maximum proton energy. Proton energies were extracted from these time measurements by using the curve given in Fig. 15. The results for this shot are compared with averages for 12 shots in Table 1. We conclude that a proton energy of 5 MeV is characteristic of this experiment.

The Rh-activation detector measurement for shot 2978 indicated a neutron yield of 4.3×10^{11} neut/sr at 155°. This shot gave the largest yield, which can be compared to an average of 2.8×10^{11} neut/sr for 18 shots. The larger yield may be due in part to the higher than average proton energy on this shot. With no LiCl, the neutron yield was only $0.5 - 1.0\times10^{10}$ neut/sr. In this case, neutron production presumably results from ion bombardment of the aluminum witness plate and cathode.

Proton intensities were determined from the neutron intensities using known nuclear reaction yields. Thick-target yields for $^{7}Li(p,n)^{7}Be$ reaction on a LiCl target were calculated using published cross sections[14] and stopping powers.[15] The results are displayed in Fig. 27. These curves

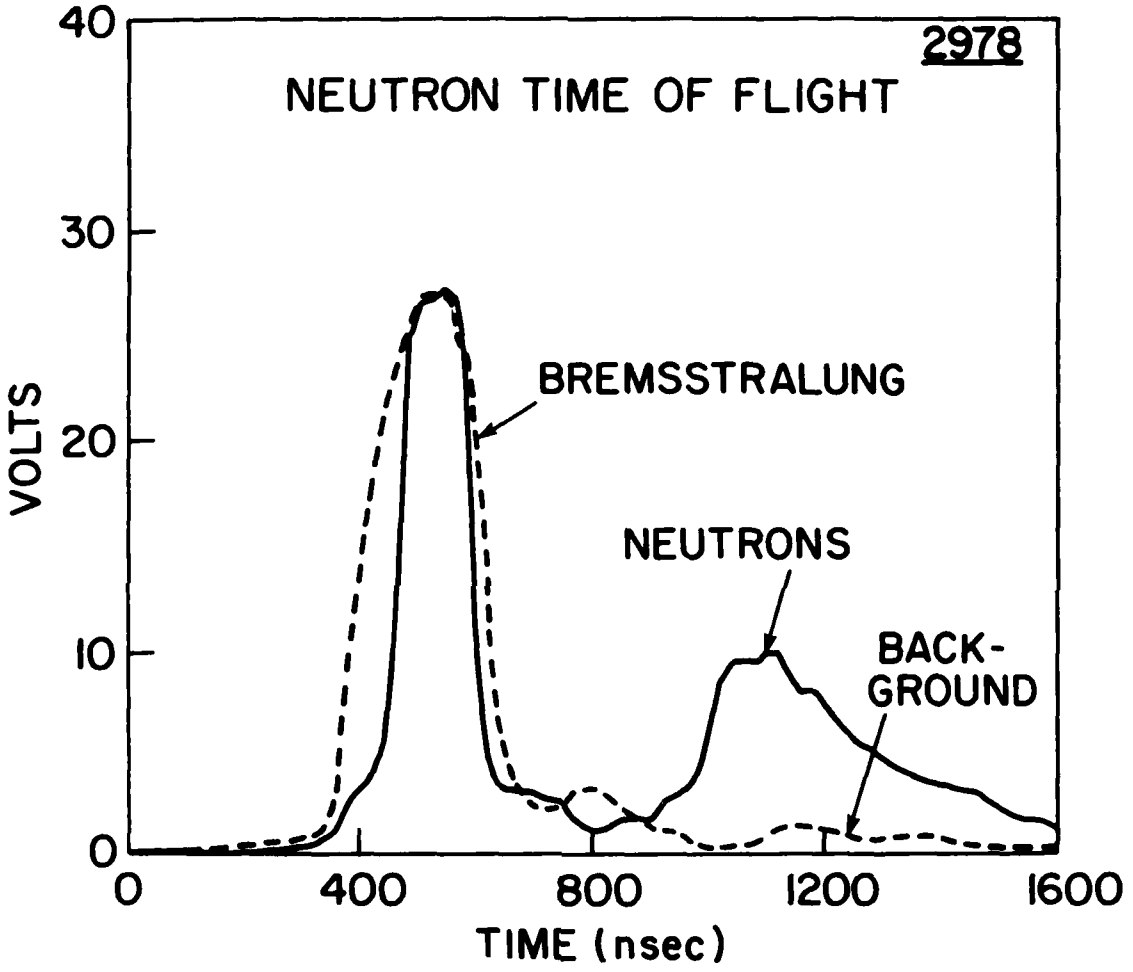

Fig. 26 — Neutron time-of-flight traces measured for shot 2978 and for a shot without a LiCl target

TABLE 1

PROTON ENERGIES FROM NEUTRON TOF

TIMING PROCEDURE	SHOT 2978	AVG OF 12 SHOTS	
	E	E	RANGE
	MeV	MeV	MeV
Peak to Peak	4.6	4.4	4.0 - 5.5
Peak to 50% Rise	5.9	5.2	4.6 - 5.9

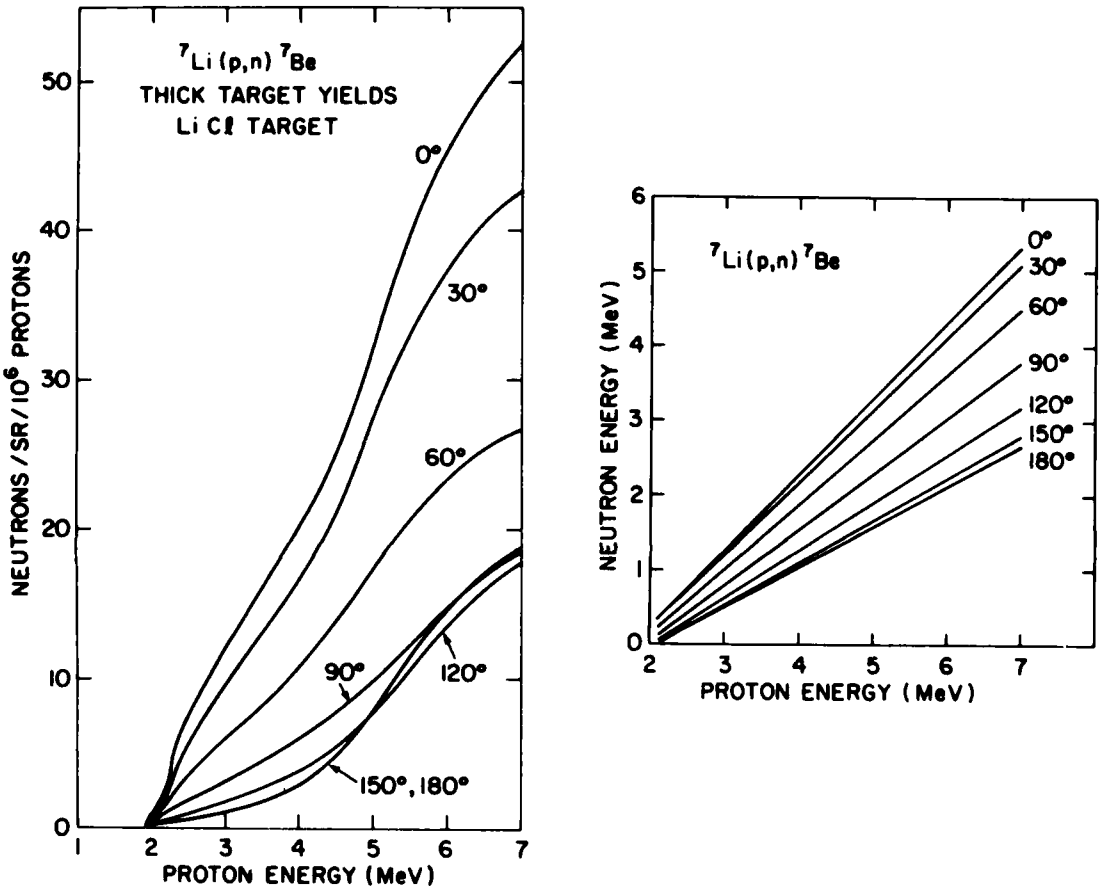

Fig. 27 — Thick target yields for the ^{7}Li(p,n)^{7}Be reaction on a LiCl target (left) and reaction kinematics for the ^{7}Li(p,n)^{7}Be reaction (right)

include only the ground-state reaction. The contribution from the first excited state is less than 10% at these energies. Note that this reaction has a threshold at 1.9 MeV and that the reaction yield is forwarded peaked. The kinematics for this reaction are also displayed in Fig. 27. For 5-MeV protons, neutron energies ranging from 1.6 to 3.3 MeV can be expected depending on the angle of the detector. For shot 2978, the observed neutron output corresponds to 5.4×10^{16} protons at 5 MeV. This result is relatively sensitive to the proton energy and ranges from 3.1×10^{16} protons at 5.9 MeV (maximum energy from TOF) to 8.1×10^{16} protons at 4.6 MeV (average energy from TOF). For all 18 shots, the average number of protons is 3.7×10^{16}. We conclude that up to $\sim 5\times10^{16}$ protons are produced with energies of $\sim$ 5 MeV.

Results from the shadowbox recessed 10.5 cm inside the cathode are shown in Fig. 28. The damage patterns produced by ions on the witness plate are outlined. These images are projected by straight-line trajectories through the corresponding witness plate apertures back toward the anode-cathode region. Ions observed at larger radii in the shadowbox appear to come from a common source which is nearer the anode than that for ions observed at smaller radii. The ions appear to come from the central region of the anode. The projections at different radii suggest that ion-focusing is going on within the anode-cathode gap with a significant fraction of the ions crossing the axis several centimeters in front of the anode.

2. Cathode Activations

Radioactivity induced on the cathode after a shot could not be understood solely by proton bombardment, but required the presence of an energetic carbon component in the beam. A pulse-height spectrum of the delayed γ-ray activity measured on the aluminum cathode with a cylindrical 7.6-cm diameter by 7.6-cm NaI detector is shown in Fig. 29. Invariably,

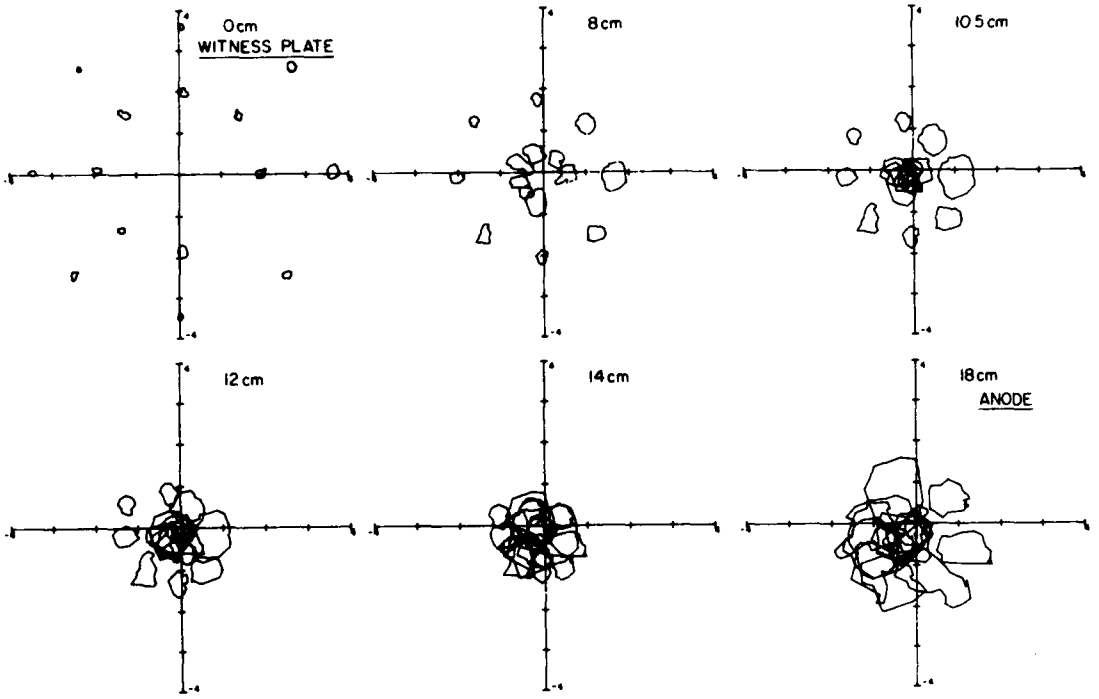

Fig. 28 — Projections of the ion damage observed on a shadowbox witness plate back through the shadowbox apertures toward the anode. The observed witness-plate damage is outlined at 0 cm. The projections at 8 cm and 10.5 cm from the witness plate indicate that ions at the smaller radius are converging faster than ions at the larger radius. The inner-radius projections pass through an apparent best focus at 10.5 cm and begin to diverge as one approaches the anode located at 18 cm. The outer-radius projections have an apparent best focus very near the anode plane.

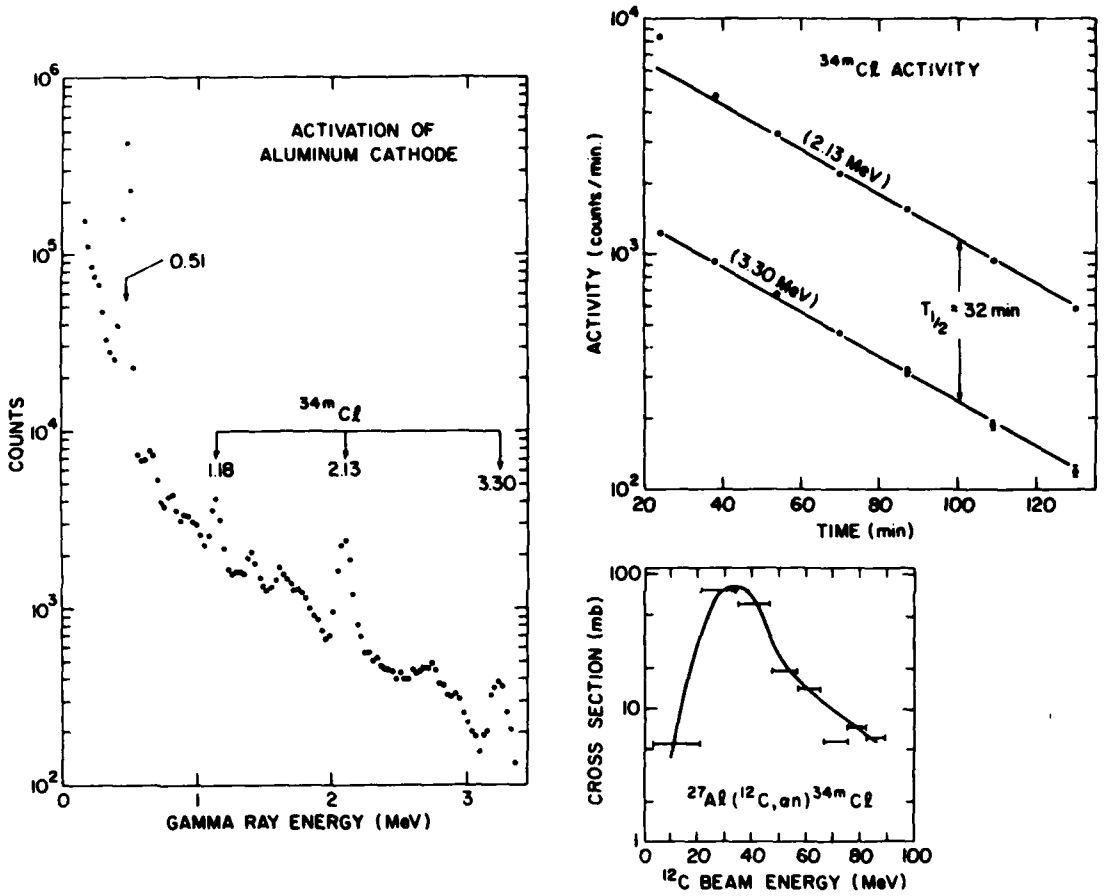

Fig. 29 — A spectrum (left) of the delayed γ-lines of 2.13 and 3.30 MeV which are observed to decay with a half-life of 32 min characteristic of ^{34m}Cl (top right). This activity can be produced by carbon-ion bombardment of the aluminum cathode as indicated by the cross section for the $^{27}Al(^{12}C,\alpha n)^{34}Cl$ reaction (lower right).

the most intense γ-ray observed was annihilation radiation (0.51 MeV) resulting from positron activity produced by a variety of nuclear reactions. The decay of this γ-ray could not be characterized by a single half-life. The γ-rays at 1.18, 2.13 and 3.30 MeV dominate the high energy region of this spectrum. A half-life of 32 min. was measured for the decay of 2.13 and 3.30 MeV γ-rays, as shown in Fig. 29. These results indicate that this activity is ^{34m}Cl. This identification was confirmed by Ge-spectroscopy of the cathode activity, as summarized in Table 2. Gamma-ray energies were measured to a precision of $\pm$ 1 keV, and the values agree with those recommended from the literature for ^{34m}Cl. Note that the intense 146-keV γ-ray from ^{34m}Cl was observed by Ge-spectroscopy, but not in the NaI spectrum (see Fig. 29). In addition, γ-rays associated with ^{63}Zn and ^{7}Be were also observed. The ^{7}Be activity results from the ^{7}Li(p,n)^{7}Be reaction in the LiCl target. The ^{63}Zn activity results from the ^{63}Cu(p,n)^{63}Zn reaction on a copper impurity in the aluminum cathode. No other γ-activities were observed in these measurements. The ^{34m}Cl activity cannot be accounted for by a proton-induced reaction but can result from the ^{27}Al(^{12}C,αn)^{34m}Cl reaction due to a carbon component in the ion beam. The cross section[16] for this reaction is given in Fig. 29. If the carbon ions were produced in the 6+ charge state and accelerated through 5 MV to give an energy of 30 MeV, the number of ions required to account for the maximum observed activity would be 3×10^{14}. For lower energy ions, the number increases because the cross section for this reaction decreases with energy. Also, this value represents a lower limit because activity blown off the cathode during the shot is not measured. We conclude that more than 3×10^{14} carbon ions per shot are generated in these experiments.

TABLE 2

Ge - Spectroscopy of Aluminum Cathode

Observed Gamma Lines (keV)	Recommended Gamma Energies (keV)	Radionuclide	Source Reaction	Threshold Energy (MeV)
3303	3303.5[a]	^{34m}Cl	$^{27}Al(^{12}C,\alpha n)^{34m}Cl$	4.9
2127	2127.5[a]			
1176	1175.8[a]			
510	511.0[b]			
145.7	145.7[c]			
669	669.6[d]	^{63}Zn	$^{63}Cu(p,n)^{63}Zn$	4.2
961	961.9[d]			
477	477.6[b]	^{7}Be	$^{7}Li(p,n)^{7}Be$	1.9

[a] R. W. Kavanagh, A. Gallmann, E. Aslanides, F. Jundt, and E. Jacobs, Phys. Rev. 175, 1426 (1968).

[b] J. B. Marion, Nuclear Data A4, 301 (1968).

[c] T. F. Ward and P. K. Kuroda, J. Inorg. Nucl. Chem. 33, 609 (1971).

[d] R. Colle, R. Kishore, and J. B. Cumming, Phys. Rev. C9, 1819 (1974).

The activation of the cathode was also measured on a shot where the aluminum cathode was replaced by a stainless steel cathode. The γ-ray pulse-height spectrum obtained in this case is shown in Fig. 30. There is no evidence for the ^{34m}Cl activity when the aluminum cathode is removed. This observation supports the previous conclusion that the ^{34m}Cl activity results from the bombardment of aluminum by energetic carbon ions. The only prominent feature in the spectrum in Fig. 30, except for annihilation radiation, is a 1.43-MeV γ-ray which decays with a half-life of 22 min. This activity is characteristic of ^{52m}Mn which can be produced by the ^{52}Cr(p,n)^{52m}Mn reaction on the 18% chromium component in the stainless steel. The thick-target yield[17] for this reaction, which has a threshold at 5.9 MeV, is shown in Fig. 31. The presence of this activity indicates that protons exceeded 5.9 MeV on this shot. For a proton energy of 6.5 MeV, only $\sim 5\times10^{14}$ protons are required to account for the measured ^{52m}Mn activity. This is only $\sim$ 2% of the number of protons measured on this shot by the ^{7}Li(p,n)^{7}Be diagnostic. Therefore, the ^{52m}Mn activity can be accounted for by a small fraction of the proton beam exceeding the 5.9-MeV threshold for producing this activity.

3. Variation of Diode Parameters

In the course of the 25 shots comprising this experiment, the behavior of the diode was studied for several different variations of diode parameters. These studies included variations of the anode-cathode gap, the number of prepulse insulators, and the anode structure.

The AK gap study consisted of 5 shots with gaps ranging from 2.8 cm to 7.0 cm. For gaps >4.8 cm, the voltage and current traces did not change significantly with the gap spacing. For gaps <4 cm the voltage risetime and peak value did not change, but the voltage decayed more rapidly after

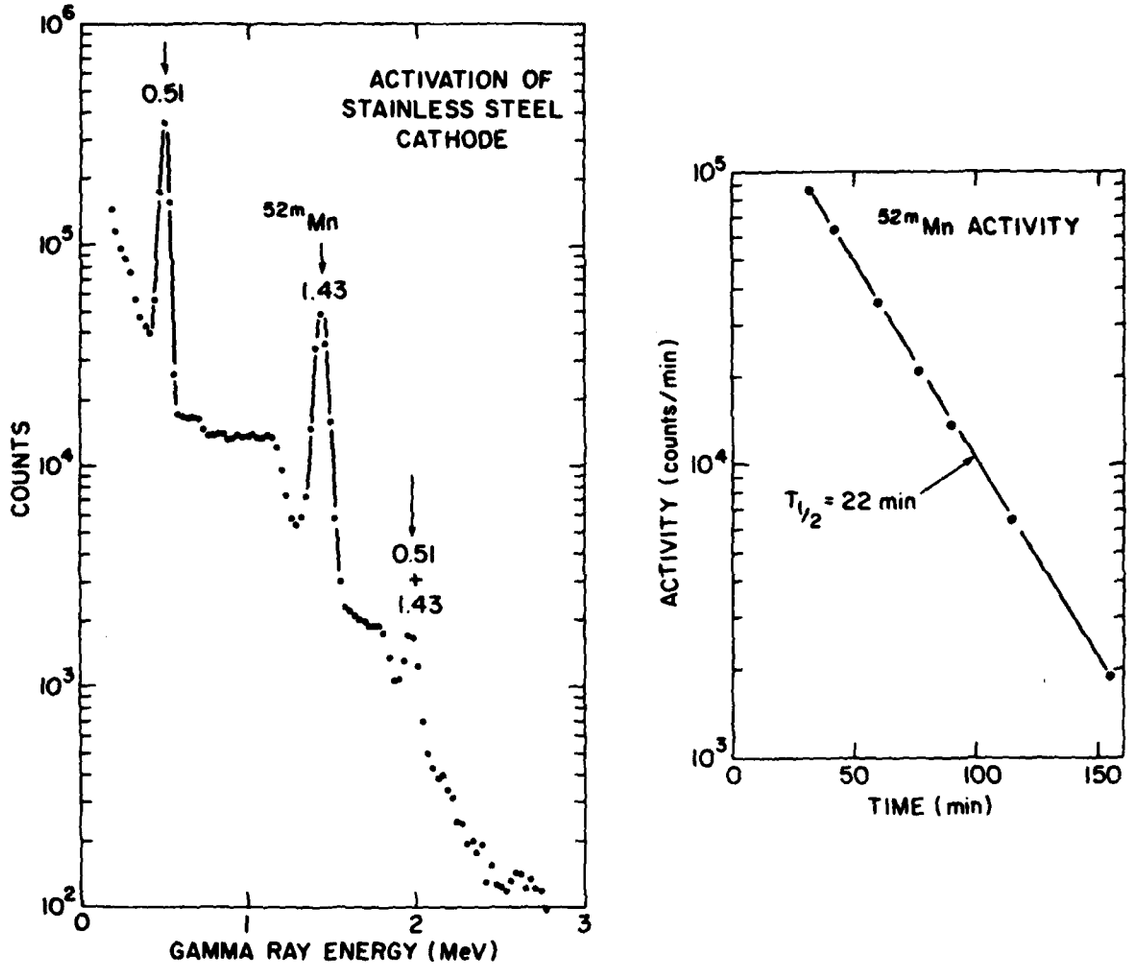

Fig. 30 — A spectrum of the delayed γ-ray activity (left) measured on a stainless steel cathode shows a 1.43-MeV γ-line which decays with a 22-min half-life characteristic of ^{52m}Mn (right)

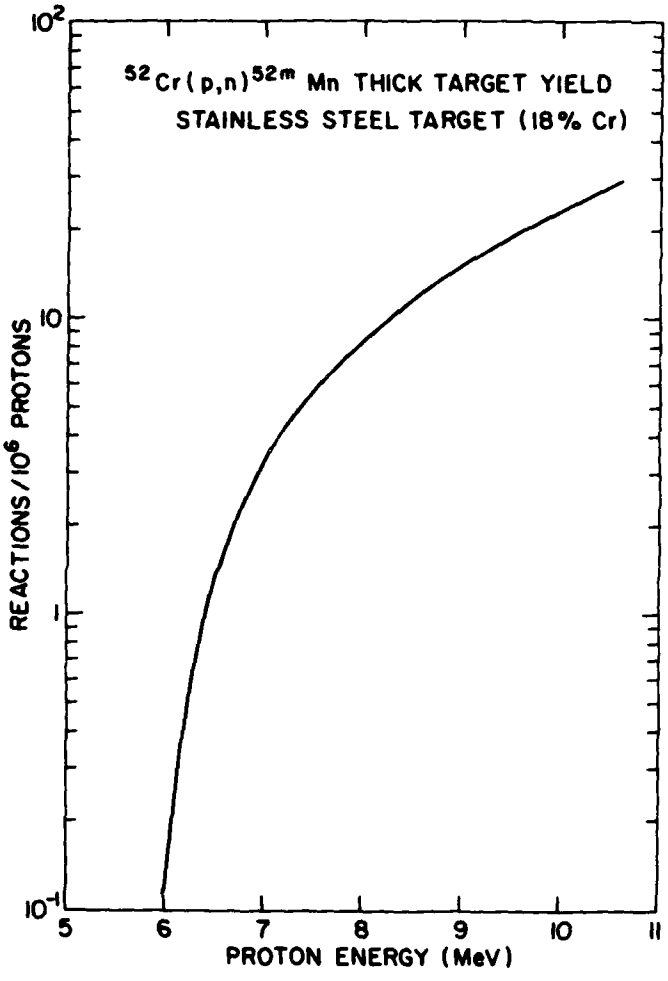

Fig. 31 — The thick target yield for the ^{52}Cr(p,n)^{52m}Mn reaction on a stainless steel target

the peak. For example, the full width at half maximum of voltage V_B dropped from ~ 160 ns for gaps ≥4.8 cm to ~ 100 ns for a 2.8-cm gap. Likewise the peak current as measured by I_T was 30 kA higher for the small gap. These observations indicate that the diode impedance is falling rapidly during the latter half of the pulse. The ion diagnostics showed a decrease in the number of neutrons and ^{34m}Cl nuclei produced for smaller gaps as indicated in Fig. 32. The decrease in neutron and ^{34m}Cl production may be due to either the production of fewer ions or to a reduced voltage across the diode. In the latter case, the strong energy dependence of the cross sections for these diagnostics causes the reduced outputs. The ion intensity cannot be unfolded from these diagnostics until better voltage and current measurements are available and direct ion current measurements are made.

One constraint on the efficient coupling of a low impedance diode to the Aurora generator is the presence of a diode prepulse. A prepulse can cause anode and cathode plasmas to form and begin to close the diode gap. As a consequence, the diode may short out prematurely when the main pulse is impressed on the diode. A 300-nsec long prepulse of ~ 100-kV peak voltage appears on the vacuum transmission line 1.5 μsec before the main voltage pulse. This prepulse could be a source of premature plasma formation in the diode region. To minimize this effect, an insulator flashover switch was located behind the cathode to capacitively attenuate the prepulse level at the diode. By changing the number of insulators, the prepulse voltage could be decreased by an order of magnitude. Shots were taken with 0, 2, 4 and 6 insulators in this switch, for a 5-cm AK gap. The diode behavior showed no difference between four to six insulators. For 2 insulators, the rise of the voltage to its peak did not change

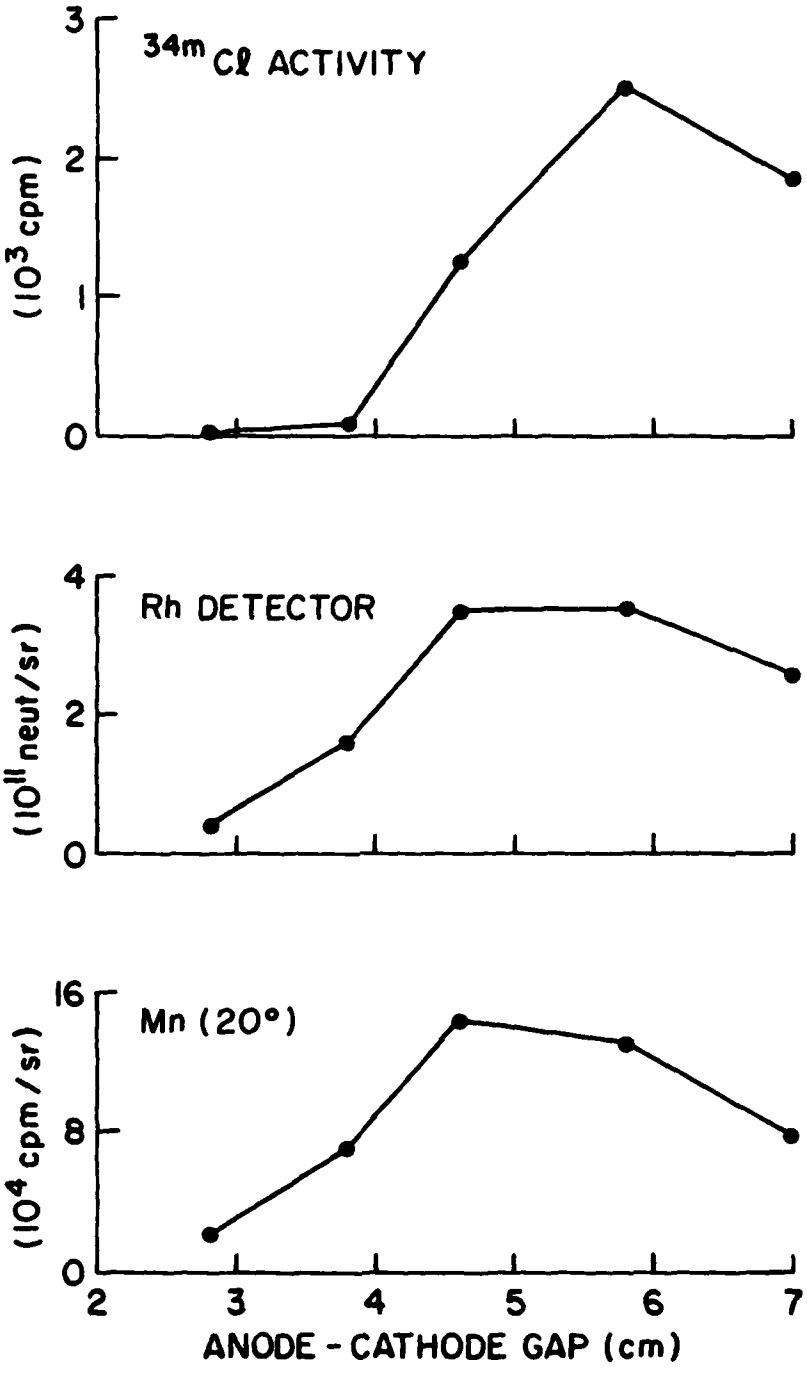

Fig. 32 — Dependence of the cathode activation (^{34m}Cl) and the $^{7}Li(p,n)^{7}Be$ neutron production (Rh and Mn detectors) on the anode-to-cathode gap.

significantly, but after the peak, the voltage collapsed rapidly. For zero insulators (no prepulse switch), the voltage risetime increased, the peak voltage decreased by ~ 1 MV and a rapid decay followed the peak and shortened the pulses to 135 nsec (FWHM). For the configurations with zero and two insulators, peak diode currents of ~ 230 kA were well above the average of 190 kA for the entire run, indicating lower impedance operation of the diode. The dependence of the ion diagnostics on the number of insulators in the prepulse switch is shown in Fig. 33. The decrease in neutron and Cl^{34m} production is consistent with gap closure due to plasma production lowering the diode voltage.

Ion production in these experiments depends on the interaction of electrons with the anode foil. Reflexing of electrons through the anode foil may enhance ion production. In these negative-polarity experiments, the CH_2 anode foil acts as a ground plane as well as a plasma source for ions (see Fig. 13). Electrons from the cathode may reflex through the anode foil due to the magnetic field produced by current in the anode stalk. The gyroradius of 5-MeV electrons in the magnetic field at the cathode radius resulting from a 150-kA current is ~ 3 cm. For an anode stalk longer than 3 cm, electrons can reflex through the anode without interacting with the aluminum plate supporting the anode. In addition, a virtual cathode may be formed in the vacuum region behind the support plate and reflect electrons back toward the anode. These two potential reflexing mechanisms complement one another.

Several shots with different anode structures were made to examine the role of electron reflexing in the diode. First, a series of shots with anode stalk lengths ranging from 3 to 12.8 cm was made for AK gaps of 5 cm. No significant differences in the voltage, current, neutron

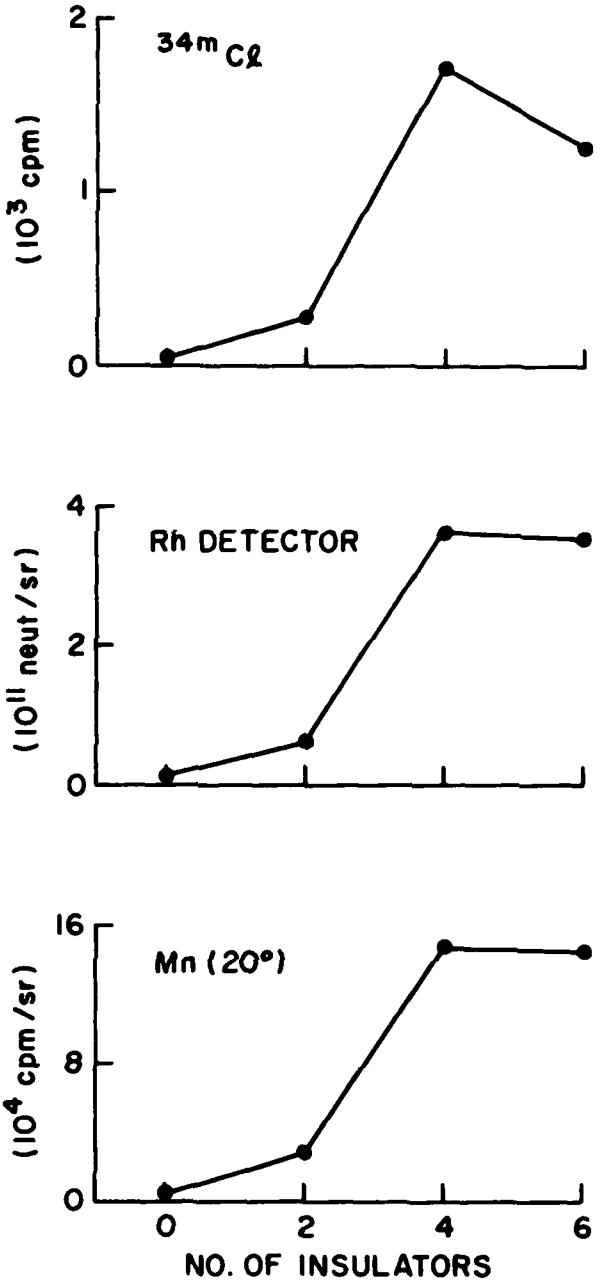

Fig. 33 — Dependence of the cathode activation (^{34m}Cl) and the ^{7}Li(p,n)^{7}Be neutron production (Rh and Mn detectors) on the number of prepulse insulators.

output and ^{34m}Cl production were observed. X-ray pinhole images indicated that the longer stalks were radiating along almost their entire length. This suggests that current is being conducted along the anode stalk to the aluminum support plate. Finally, three shots were taken with the anode foil placed directly on the support plate as indicated in Fig. 34. Shot 1 is identical to the previous shots except it has no anode stalk. Shot 2 has a CH_2 foil with no aluminum backing plate. Electron reflexing through the anode is possible in these two shots. Shot 3 has a 13-mm thick carbon plate behind a 3-mm thick aluminum support plate to suppress electron reflexing. The neutron yield on shot 3 is about one-half of that on shots 1 and 2 as indicated by the Mn activity at 90° and 20°. The Rh-counter activity scales with the 90° Mn-foil activity. The thicker anode on shot 3 attenuates the neutron intensity toward the Rh counter by about 20%. A comparison of the neutron yields at 20° and 90° indicates that the angular distribution is forward-peaked, as expected from the yield curves see Fig. 27. These shots indicate that if electron reflexing is enhancing the ion production, it is not the dominant effect.

V. SUMMARY OF RESULTS

The ion diode experiments on Aurora described in this paper have produced up to 5×10^{16} protons with energies of $\sim$ 5 MeV and pulse durations of $\leq$ 150 ns. The corresponding average proton current exceeds 50 kA or 20% of the total current. These numbers give $\sim$ 40-kJ energy in the proton beam. The $\sim$ 20% ion generation efficiency compares favorably with computer simulations. In addition to protons, a carbon-ion component of greater than 3×10^{14} ions was extracted from the CH_2 anode foil. The energy of these ions was not determined, but their number may be larger depending on their charge-state and hence their energy.

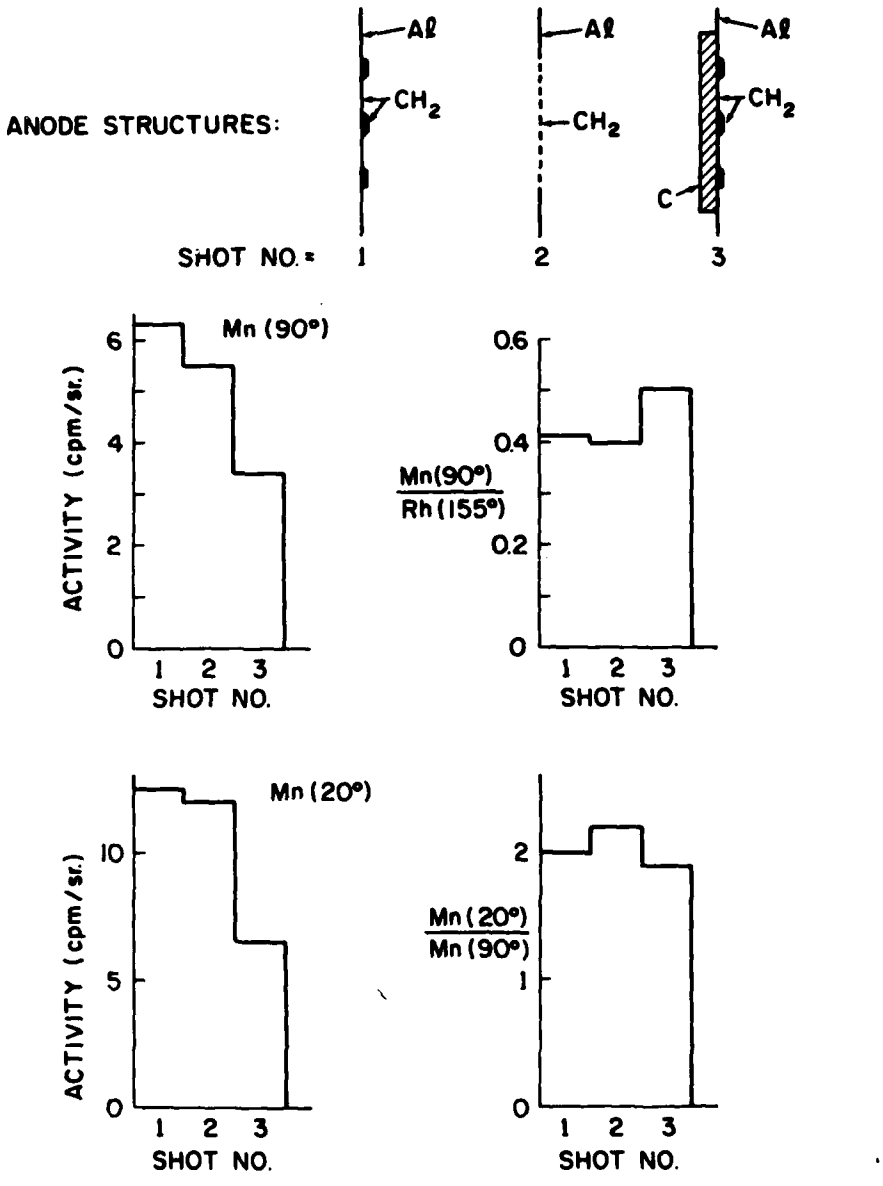

Fig. 34 — Comparisons of neutron measurements for three shots (1, 2 and 3) with different anode structures.

The enhancement of the ion production efficiency over the child-Langmuir limit may be due to increased electron lifetime in the diode. Previous experiments[1] with pinch reflex diodes have indicated enhanced ion production can result from electron reflexing through an anode foil. However, it was demonstrated that electron reflexing is not the dominant effect in the present experiments. Experimentally, the electron beam pinches on the anode, and the ions appear to originate primarily from a small area (2-4 cm^2) on the anode axis. Both of these results are supported by the computer simulation. Moreover, the simulation indicates that electrons in the diode undergo complicated figure-eight-like orbits. The relatively slow gap crossing due to electron ∇B drift motion is consistent with the observed ion efficiency.

Ion images and trajectories from the shadowbox measurements suggest that the ions have a relatively large divergence from a localized region on axis within the anode-cathode gap. This result suggests some focusing mechanism at work in the diode. These observations are consistent with the computer simulation.

Experiments with various prepulse switches and AK gaps indicate that the diode is sensitive to the prepulse voltage level (25 kV < Vpp < 200 kV). There was some indication that gap closure may have occurred late in the pulse for small AK gaps (< 4 cm) or for large prepulse levels. Such closure may be caused by anode or cathode plasmas produced by the prepulse which occurs ~ 1.5 μs before the main voltage pulse.

Several new diagnostic techniques were developed and applied successfully in the course of these experiments. The use of the $^7Li(p,n)^7Be$ reaction with LiCl targets as a neutron source for protons of ~ 5 MeV was demonstrated. Neutron intensity measurements by Mn-activation proved to

be a viable technique. An independent absolute calibration of this detection technique would be very useful. A nuclear reaction for detecting carbon ions, namely $^{27}Al(^{12}C,\alpha n)^{34m}Cl$, was used successfully. Additional measurements of the cross section for this reaction below 30 MeV are needed.

The continuing experimental program has focused on reversing the accelerator polarity to permit ion beam extraction, improvements of the ion and accelerator diagnostics, and improvement of power flow to the diode.

ACKNOWLEDGMENTS:

The authors would like to acknowledge a preliminary computer simulation performed by Roswel Lee which provided the impetus for performing the initial experiments as well as the invaluable technical assistance of J. Negri and T. Robinson at the Naval Research Laboratory and D. Whittaker, C. Casaers, T. Cassidy, A. Pourier and the entire Operations and Maintenance crew at the Harry Diamond Laboratories.

REFERENCES

1. G. Cooperstein, Shyke A. Goldstein, D. Mosher, R. J. Barker, J. R. Boller, D. G. Colombant, A. Drobot, R. A. Meger, W. F. Oliphant, P. F. Ottinger, F. L. Sandel, S. J. Stephanakis and F. C. Young, "NRL Light Ion Beam Research for Inertial Confinement Fusion", Fifth Workshop on Laser Interaction and Related Plasma Phenomena, Laboratory for Laser Energetics, Rochester, New York, November 5-9, 1979.

2. P. A. Miller, D. J. Johnson, T. P. Wright, and G. W. Kuswa, Comments Plasma Phys. 5, 95 (1979).

3. Shyke A. Goldstein and R. Lee, Phys. Rev. Lett. 35, 1079 (1975).

4. S. Stephanakis, J. R. Boller, G. Cooperstein, Shyke A. Goldstein, D. D. Hinshelwood, D. Mosher, W. F. Oliphant and F. C. Young, Bull. Am. Phys. Soc. 24, 1031, (1979).

5. G. Cooperstein, J. R. Boller, Shyke A. Goldstein, D. Mosher, W. F. Oliphant, S. J. Stephanakis, F. C. Young, R. D. Genuario and J. E. Maenchen, IEEE Conference Record-Abstract, 1980 Intl. Conf. on Plasma Science, Madison, Wisconsin (1980), p. 97.

6. D. G. Colombant, Shyke A. Goldstein, D. Mosher, Phys. Rev. Lett. 45, 1253 (1980).

7. D. Mosher, D. G. Colombant, Shyke A. Goldstein, to be published in Comments on Plasma Physics and Controlled Fusion, 1980.

8. S. E. Graybill, Harry Diamond Laboratories Technical Report No. 1862, (1978).

9. B. Bernstein and I. Smith, IEEE Trans. Nucl. Sci. 20, 294 (1973).

10. F. C. Young, IEEE Trans. on Nucl. Sci. NS-22, 718 (1975).

11. F. C. Young and S. J. Stephanakis, NRL Memorandum Report No. 3104, August 1975.

12. G. Huttlin, Harry Diamond Laboratories Technical Report No. 22900-80-1.

13. H. W. Koch and J. W. Motz, Rev. Mod. Phys. 31, 4 (1959).

14. H. Liskien and A. Paulsen, Atomic and Nuclear Data Tables 15, 57 (1975).

15. H. H. Andersen and J. F. Ziegler, The Stopping and Ranges of Ions in Matter, Vol. 3 (Pergamon Press, NY, 1977).

16. I. Landenbauer-Bellis, I. L. Preiss and C. E. Anderson, Phys. Rev. 125, 606 (1962).

17. F. C. Young, S. J. Stephanakis, and D. Mosher, J. Appl. Phys. 48, 3642 (1977).

DISTRIBUTION LIST

Director
Defense Intelligence Agency
Washington, DC 20301

Attn: DTICI Robert I. Rubenstein — 1 copy

Defense Advanced Research Project Agency
1400 Wilson Blvd.
Arlington, VA 22209
Attn: R. Bayless — 1 copy

Director
Defense Nuclear Agency
Washington, DC 20305

Attn:		
	FCPR	1 copy
	STVL	1 copy
	TISI Archives	1 copy
	TITL Tech. Library	3 copies
	J. Z. Farber (RAEV)	1 copy
	R. L. Gullickson (RAEV)	1 copy

Defense Technical Information Center
Cameron Station
5010 Duke Street
Alexandria, VA 22314

Attn: T. C. — 12 copies

Under Sec'y of Defense for RSCH and ENGRG
Department of Defense
Washington, DC 20301

Attn: S&SS(OS) — 1 copy

Chief
Livermore Division Fld Command DNA
Lawrence National Laboratory
P. O. Box 808
Livermore, CA 94550

Attn: FCPRL — 1 copy

National Technical Information Service
U.S. Department of Commerce
5285 Port Royal Road
Springfield, VA 22161 — 24 copies

Commander
BMD System Command
P. O. Box 1500
Huntsville, AL 35807

Attn: SSC-TEN — 1 copy

DEP Chief of Staff for RSCH DEV & ACQ
Department of the Army
Washington, DC 20310

Attn: DAMA-CSM-N — 1 copy

Commander
Harry Diamond Laboratories
2800 Powder Mill Road
Adelphi, MD 20783
(CNWDI-INNER ENVELOPE: ATTN: DELHD-RBH)

Attn:		
	DELHD-NP	1 copy
	DELHD-RCC J. A. Rosado	1 copy
	DRXDO-RBH P. A. Caldwell	1 copy
	DRXDO-RBH D. Schallhorn	1 copy
	DRXDO-TI Tech Lib.	1 copy
	S. Graybill	1 copy

Commander
Picatinny Arsenal
Dover, NJ 07801

Attn: SMUPA ND-N-E — 1 copy

Commander
U. S. Army Missile Command
Redstone Arsenal, AK 35809

Attn: Redstone Scientific Information CTR
DRCPM-PM-PE-EA — 1 copy

Commander
U. S. Army Nuclear Agency
7500 Backlick Road
Building 2073
Springfield, VA 22150

Attn: ATCN-W — 1 copy

Commander
U. S. Army Test and Evaluation COMD
Aberdeen Proving Ground, MD 21005

Attn: DRSTE-EL — 1 copy

Commander
Naval Electronic Systems CMD HQS
Washington, DC 20360

Attn: Code 5032 — 1 copy

Commanding Officer
Naval Intelligence Support Center
4301 Suitland Road - Building 5
Washington, DC 20390

Attn: NISC-45 — 1 copy

Naval Research Laboratory

Addressee: Attn: Name/Code	
Code 2628 - TIC-Distribution	25 copies
Code 4020 - J. Boris	1 copy
Code 6682 - D. Nagel	1 copy
Code 4700 - T. Coffey	25 copies
Code 4707 - J. Davis	1 copy
Code 4730 - S. Bodner	1 copy
Code 4740 - V. Granatstein	1 copy
Code 4760 - B. Robson	1 copy
Code 4761 - C. Kapetanakos	1 copy
Code 4770 - Branch Head	10 copies
Code 4770 - I. Vitkovitsky	1 copy
Code 4771 - D. Mosher	10 copies
Code 4773 - G. Cooperstein	10 copies
Code 4790 - D. Colombant	1 copy
Code 4790 - I. Haber	1 copy
Code 4790 - M. Lampe	1 copy

Officer-in-Charge
Naval Surface Weapons Center
White Oak, Silver Spring, MD 20910

Attn:	
Code WR43	1 copy
Code WA501 - Navy Nuc Prgms Off	1 copy

Chief of Naval Operations
Navy Department
Washington, DC 20350

Attn: R. A. Blaise 604C4 — 1 copy

Commander
Naval Weapons Center
China Lake, CA 93555

Attn: Code 533 *Tech* Lib. — 1 copy

AF Weapons Laboratory, AFSC
Kirtland AFB, NM 87117

Attn:	
CA	1 copy
ELC	1 copy
NT	1 copy
SUL	1 copy
DYP	1 copy
J. Darrah	1 copy
W.L. Baker	1 copy

HQ USAF/RD
Washington, DC 20330

Attn: RDQSM — 1 copy

Director
Joint Strat TGT Planning Staff JCS
OFFUTT AFB
Omaha, NB 68113

Attn: JSAS — 1 copy

SAMSO/DY
Post Office Box 92960
Worldway Postal Center
Los Angeles, CA 90009
(Technology)

Attn: DYS — 1 copy

SAMSO/IN
Post Office Box 92960
Worldway Postal Center
Los Angeles, CA 90009

Attn: IND MAJ D. S. Muskin — 1 copy

SAMSO/MN
Norton AFB, CA 92409
(Minuteman)

Attn: MNNH — 1 copy

SAMSO/SK
Post Office Box 92960
Worldway Postal Center
Los Angeles, CA 90009
(Space Comm Systems)

Attn: SKF P. H. Stadler — 1 copy

U. S. Department of Energy
Division of Inertial Fusion
Washington, DC 20545

Attn:	
G. Canavan	1 copy
T. F. Godlove	1 copy
S. L. Kahalas	1 copy
R. L. Schriever	1 copy

Argonne National Laboratory
9700 South Cass Avenue
Argonne, Illinois 60439

Attn:	
G. R. Magelssen	1 copy
R. J. Martin	1 copy

Brookhaven National Laboratory
Upton, NY 11973

Attn: A. F. Maschke — 1 copy

Lawrence Berkley Laboratory
Berkeley, CA 94720

Attn: D. Keefe — 1 copy

Lawrence Livermore National Laboratory
P. O. Box 808
Livermore, CA 94550

Attn:	
L-18	1 copy
L-153	1 copy
R. O. Bangerter	1 copy
R. J. Briggs	1 copy
E. P. Lee	1 copy
J. H. Nuckolls	1 copy
S. S. Yu	1 copy
Tech Info Dept. L-3	1 copy

Los Alamos National Laboratory
P. O. Box 1663
Los Alamos, NM 87545

Attn:	
D. B. Henderson	1 copy
R. B. Perkins	1 copy
L. L. Thode	1 copy

National Science Foundation
Mail Stop 19
Washington, DC 20550

Attn: D. Berley — 1 copy

Sandia National Laboratories
P. O. Box 5800
Albuquerque, NM 87115

Attn: J. R. Freeman — 1 copy
S. Humphries — 1 copy
D. J. Johnson — 1 copy
G. W. Kuswa — 1 copy
P. S. Miller — 1 copy
J. P. Vandevender — 1 copy
G. Yonas — 1 copy
Doc Con for 3141 Sandia RPT Coll — 1 copy

AVCO Research and Systems Group
201 Lowell Street
Wilmington, MA 01887

Attn: Research Lib. A830 Rm. 7201 — 1 copy

BDM Corporation, The
795 Jones Branch Drive
McLean, VA 22101

Attn: Tech Lib. — 1 copy

Boeing Company, The
P. O. Box 3707
Seattle, WA 98124

Attn: Aerospace Library — 1 copy

Cornell University
Ithaca, NY 14850

Attn: D. A. Hammer — 1 copy
R. N. Sudan — 1 copy
J. Maenchen — 1 copy

Dikewood Industries, Inc.
1009 Bradbury Drive, SE
Albuquerque, NM 87106

Attn: L. W. Davis — 1 copy

EG&G, Inc.
Albuquerque Division
P. O. Box 10218
Albuquerque, NM 87114

Attn: Technical Library — 1 copy

Ford Aerospace & Communications Operations
Ford & Jamboree Roads
Newport Beach, CA 92663
(Formerly Aeronutronic Ford Corporation)

Attn: Tech Info Section — 1 copy

Ford Aerospace & Communications Corp
3939 Fabian Way
Palo Alto, CA 94303
(Formerly Aeronutronic Ford Corporation)

Attn: Library — 1 copy
D. R. McMorrow MS G 30 — 1 copy

General Electric Company
Space Division
Valley Forge Space Center
Goddard Blvd., King of Prussia
P. O. Box 8555
Philadelphia, PA 19101

Attn: J. C. Penden VFSC, Rm. 4230M — 1 copy

General Electric Company
Tempo-Center for Advanced Studies
816 State Street (P. O. Drawer QQ)
Santa Barbara, CA 93102

Attn: DASIAC — 1 copy

Grumman Aerospace Corporation
Bethpage, NY 11714

Attn: P. Suh — 1 copy

Institute for Defense Analyses
400 Army-Navy Drive
Arlington, VA 22202

Attn: IDA Librarian R S. Smith — 1 copy

Ion Physics Corporation
South Beford Street
Burlington, MA 01803

Attn: H. Milde — 1 copy

IRT Corporation
P. O. Box 81087
San Diego, CA 92138

Attn: R. L. Mertz — 1 copy

JAYCOR, Inc.
205 S. Whiting Street
Alexandria, VA 22304

Attn: J. Guillory — 1 copy
R. Hubbard — 1 copy
R. Sullivan — 1 copy
D. A. Tidman — 1 copy

JAYCOR, Inc.
1401 Camino Del Mar
Del Mar, CA 92014

Attn: E. Wenaas — 1 copy

JAYCOR, Inc.
300 Unicorn Park Drive
Woburn, MA 01801

Attn: H. Linnerud — 1 copy

Kaman Science Corporation
P. O. Box 7463
Colorado Springs, CO 80933

Attn:	A. P. Bridges	1 copy
	D. H. Bryce	1 copy
	J. R. Hoffman	1 copy
	W. E. Ware	1 copy

Lockheed Missiles and Space Co., Inc.
3251 Hanover Street
Palo Alto, CA 94304

Attn:	L. F. Chase	1 copy

MIT
Massachusetts Institute of Technology
Cambridge, MA. 02139

Attn:	R.C. Davidson	1 copy
	G. Bekefi	1 copy
	D. Hinshelwood	1 copy

Maxwell Laboratories, Inc.
9244 Balboa Avenue
San Diego, CA 92123

Attn:	R. W. Clark	1 copy
	A. C. Kolb	1 copy
	P. Korn	1 copy
	A. R. Miller	1 copy
	J. Pearlman	1 copy

McDonnell Douglas Corporation
5301 Bolsa Avenue
Huntington Beach, CA 92647

Attn:	S. Schneider	1 copy

Mission Research Corporation
1400 San Mateo Blvd. SE
Albuquerque, NM 87108

Attn:	B. B. Godfrey	1 copy

Mission Research Corporation-San Diego
P. O. Box 1209
LaJolla, CA 92038

Attn:	V.A.J. Van Lint	1 copy

Mission Research Corporation
735 State Street
Santa Barbara, CA 93101

Attn:	W. C. Hart	1 copy
	C. L. Longmire	1 copy

Northrop Corporation
Electronic Division
2301 West 120th Street
Hawthorne, CA 90250

Attn:	V. R. DeMartino	1 copy

Northrop Corporation
Northrop Research and Technology Ctr.
3401 West Broadway
Hawthorne, CA 90205 1 copy

Physics International Co.
2700 Merced Street
San Leandro, CA 94577

Attn:	J. Benford	1 copy
	B. Bernstein	1 copy
	R. Genuario	1 copy
	L. B. Goldman	1 copy
	A. J. Toepfer	1 copy

Pulsar Associates, Inc.
11491 Sorrento Valley Blvd.
San Deigo, CA 92121

Attn:	C. H. Jones, Jr.	1 copy

Pulse Sciences, Inc.
1615 Broadway, Suite 610
Oakland, CA 94612

Attn:	I. Smith	1 copy
	P. Spence	1 copy
	S. Putman	1 copy

R&D Associates
P. O. Box 9695
Marina Del Rey, CA 90291

Attn:	W. R. Graham, Jr.	1 copy
	M. Grover	1 copy
	C. MacDonald	1 copy
	E. Martinelli	1 copy

R&D Associates
Suite 500
1401 Wilson Blvd.
Arlington, VA 22209

Attn:	P. J. Turchi	1 copy

Science Applications, Inc.
P. O. Box 2351
LaJolla, CA 92038

Attn:	J. Robert Beyster	1 copy

Spire Corporation
P. O. Box D
Bedford, MA 01730

Attn:	R. G. Little	1 copy

SRI International
333 Ravenswood Avenue
Menlo Park, CA 94025

Attn:	Setsuo Ddairiki	1 copy

Stanford University
SLAC
P. O. Box 4349
Stanford, CA 94305

Attn:	W. B. Herrmannsfeldt	1 copy

Systems, Science and Software, Inc.
P. O. Box 1620
LaJolla, CA 92038

Attn:	A. R. Wilson	1 copy

Texas Tech University
P. O. Box 5404 North College Station
Lubbock, TX 79417

Attn: T. L. Simpson — 1 copy

TRW Defense and Space Sys Group
One Space Park
Redondo Beach, CA 90278

Attn: Tech Info Center/S-1930 — 1 copy
Z.G.T. Guiragossian — 1 copy
D. Arnush — 1 copy

University of California
Dept. of Physics
La Jolla, CA 92037

Attn: K. Brueckner — 1 copy

University of California
Boelter Hall 7731
Los Angeles, CA 90024

Attn: F.F. Chen — 1 copy

University of California
Irvine, CA 90024

Attn: G. Benford — 1 copy
N. Rostoker — 1 copy

University of Illinois
Urbana, IL 61801

Attn: G. H. Miley — 1 copy
J. T. Verdeyen — 1 copy

University of Rochester
Laboratory of Laser Energetics
River Station, Hopeman 110
Rochester, NY 14627

Attn: M. J. Lubin — 1 copy

University of Scranton
Dept. of Physics
Scranton, PA 18510

Attn: F. Murray — 1 copy

U. S. Department of Energy
P. O. Box 62
Oak Ridge, TN 37830 — 50 copies

Vought Corporation
Michigan Division
38111 Van Dyke Road
Sterling Heights, MI 48077
(Formerly LTV Aerospace Corp)

Attn: Tech Lib — 1 copy

Atomic Weapons Research Establishment
Building H36
Aldermaston, Reading RG 7 4PR
United Kingdom

Attn: J. C. Martin — 1 copy

Bhabha Atomic Research Centre
Bombay - 400085, India

Attn: B. K. Godwal — 1 copy
A. S. Paithankar — 1 copy

CEA, Centre de Etudes de Lemeil
B. P. 27
94190 Villeneuve, Saint George
France

Attn: A. Bernard — 1 copy
A. Jolas — 1 copy

CEA, Centre de Etudes de Valduc
P. B. 14
21120 Is-sur-Tille
France

Attn: J. Barbaro — 1 copy
C. Bruno — 1 copy
N. Camarcat — 1 copy
C. Patou — 1 copy
C. Peugnet — 1 copy

Centro Di Frascati
C.P.N. 65
00044 Frascati (Roma)
Italy

Attn: J.P. Rajer — 1 copy

Culham Laboratories
UKAEA
Ebingdon, Birks.
England

Attn: N. J. Peacock — 1 copy

Ecole Polytechnique
Labo. PMI
91128 Palaseau Cedex
France

Attn: J. M. Buzzi — 1 copy
H. Doucet — 1 copy

Institut d'Electronique Fondamentale
Universite' Paris XI-Bat. 220
F91405 Orsay
France

Attn: G. Gautherin — 1 copy

Institut Fur Neutronenphysik
un Reaktortechnik
Postfach 3640
Kernforschungszentrum
D-7500 Karlsruhe 1
West Germany

Attn: H. U. Karow — 1 copy
W. Schmidt — 1 copy

END

DATE
FILMED

4-81

DTIC